Preface

The present work is a master's thesis in material science in accordance with TMT4905 at NTNU in Trondheim. It is the end of five year study program in material science (MTMT) with specialization in materials for energy technology.

The work has been conducted during the spring of 2019 at the Institute for Energy Technology (IFE) in collaboration with the department for Battery Technology. Part of the experimental work reported here was initiated August 2018, but the work does not build on the author's project report. Some of the results reported herein have been published in ACS Applied Energy Materials titled "Silicon Nanoparticle Ensembles for Lithium-Ion Batteries Elucidated by Small-Angle Neutron Scattering" where the author of the present work is a co-author.

All work presented have been performed by the author with the exception of some of the SEM-images and the BET testing. Some of the SEM images were captured by Alexey Y. Koposov from IFE and Samson Y.Lai from IFE. The BET testing was performed by Marius U. Nagell from IFE.

Abstract

Silicon has shown large promise as an alternative to graphite anodes in lithium-ion batteries. The theoretical specific energy capacity of silicon is almost an order of magnitude larger, and silicon is vastly abundant and produced at large scales. The problem is that the specific energy capacity rapidly fades during cycling especially at high charging or discharge rates. This problem is due to a large volume increase during cycling and the low conductivity of silicon.

In the present work two methods for mitigating these issues are investigated: ball milling and carbon coating. The ball milling behavior of different types of silicon was investigated during ball milling in air. After ball milling the treated silicon was investigated using BET analysis and cells were created to compare cyclability and specific energy capacity across silicon types. A carbon coating method adapted from Meng *et al.* [1] and Lu et al. [2] were implemented using phenol as a monomer. It was attempted on pristine and ball milled particles. The ratio of Si:polymer was varied in an attempt to identify an optimal monomer amount. The particles were investigated using SEM and STEM imaging and cells were created for cycling and rate testing.

The ball milling investigation indicated that the ball milling behavior of silicon is highly dependent on the specific properties of the silicon type. Ball milling of amorphous silicon likely causes the formation large amounts of silicon oxide which are detrimental to battery performance. Silicon particles were partially covered in carbon which adhered to the surface, but clear confirmation of a complete coating were not found.

Sammendrag

Silisium har vist stort potensial som et alternativ til grafitt anoder for litium-ion batterier. Den teoretiske spesifikke energien til silisium er nesten ti ganger større, silisium er lett tilgjengelig, og produseres allerede på en stor skala. Problemet er at den høye spesifikke energien raskt forsvinner ved ladning og utladning av batteriet, særlig ved raks ladning og utladning. Dette problemet skyldes primært stor volumendring under ladning og den lave konduktiviteten til silisium.

I dette arbeidet undersøkes to metoder for å begrense disse probleme; kulemølling og karbon belegg. Kulemølling atferden til ulike typer silisium ble undersøkt ved kulemølling i luft. Etter kulemølling ble det behandlede silisiumet undersøkt med BET analyse og batterier ble laget for å sammenlikne stabilitet og spesifikk energikapasitet på tvers av silisium typer. En metode for å legge karbon belegg på silisium fra Meng *et al.* [1] og Lu *et al.* [2] ble implementert med fenol som monomer. Metode ble forsøkt på kulemøllede og ubehandlede partikler. Masseforholdet mellom silisium og polymer ble variert i et forsøk på å identifisere den optimale mengden monomer. Partiklene ble undersøkt, etter å ha blitt dekket med et karbon belegg, ved hjelp av SEM og STEM bilder. Batterier ble laget for å teste stabilitet og ulike ladningshastigheter.

Kulemøllings forsøkene indikerte at kulemøllings oppførselen til silisium avhenger i stor grad av de spesifikke egenskapene til typen silisium som anvendes. Kulemølling av amorft silisium forårsaker sannsynligvis formasjon av store mengder silisiumoksid som degraderer batteriegenskapene signifikant. Silisium partikler ble delvis dekket med karbon, men klare bekreftelser på dannelsen av et dekkende lag ble ikke funnet.

Acknowledgements

First, I would like to thank my supervisors for their guidance and encouragement during the experimental and writing process. Samson Y. Lai at IFE I would like to thank for his perfect combination of approachability and knowledge, Alexey Y. Koposov at IFE for his valuable input, and Kjell Wiik at NTNU for his advice and corrections.

I would like to thank the entire Battery Technology department at IFE for kindly including me in their meetings and discussions, taking part in these activities has been a great learning experience. In particular I would like to thank Marius Uv Nagell for letting me use the Ampere laboratory and Bent Thomassen for allowing me to use the SOL laboratory.

A special thanks to my grandmother, Hilde Sejersted and Jon Elster for letting me live in their house during the last semester.

Lastly, but most importantly I would like to thank the people closest to me. My friends, my mother, and my father for supporting me from afar, and always encouraging me! Especially, I would like to thank my better half Amalie Berg for her endless support and lighting up my days in times of trouble, and always.

Glossary

LIB Lithium-Ion Battery. 1, 4, 6–9, 11, 20

SEI Solid-Electrolyte Interphase. 4, 5, 9–11, 14–18, 21, 23, 42, 44, 46

CE Coulombic Efficiency. 4, 14, 23, 31, 38, 42, 44, 46

C-rate Charge-rate. 4, 7, 14, 15, 18, 21, 23, 27, 29, 38, 44, 45, 47

ICL Irreversible Capacity Loss. 4, 15–17, 23, 37, 38, 44

RCL Reversible Capacity Loss. 5

OCV Open Circuit Voltage. 5, 29

EU European Union. 6

NiMH Nickel Metal Hydride. 6

LTO Lithium Titanium Oxide. 9

LiFSI Lithium bis(fluorosulfonyl)imide. 9

EC Ethylene Carbonate. 9

DMC Dimethyl Carbonate. 9

PC Propylene Carbonate. 9

VC Vinylene Carbonate. 9

NASICON Sodium Super Ionic Conductor. 9

LiEDC Lithium ethylene glycol dicarbonate. 10

PSD Particle Size Distribution. 15, 16

PVDF Polyvinylidene Diflouride. 20, 21

PAA Polyacrylic Acid. 20, 21

CMC Carboxymethyl Cellulose. 20, 21, 26, 27

SEM Scanning Electron Microscopy. 30, 34, 43, 44

BET Brunauer-Emmett-Teller. 30, 31, 42, 53

STEM Scanning Transmission Electron Microscopy. 30, 43

Contents

List of Figures

List of Tables

1 Introduction

Global warming is one of the primary global concerns and potential existential threats facing our modern society. The emission of greenhouse gases have to be limited to preserve the climate that we, and our civilizations, have adapted to and thrived in. In order to achieve limited emissions the dependence on fossil fuels must be eliminated. The European Commission operates with a maximum temperature increase of $2\,°C$ and a stated goal of limiting temperature increase to $1.5\,°C$. This will require a substantial change to our societies. How we travel, what we eat, how we produce energy, and how we store energy all has to be revolutionized. Green energy production in the form of solar cells and wind turbines are being researched and developed at an accelerating pace. Common for these energy sources is that they convert natural phenomena into electricity and that they produce energy with a high variance which does not reflect the variance in energy consumption. This requires the construction of a highly intelligent and adaptable energy grid. An essential part of such a system will be the batteries storing large amounts of energy, both in the electric grid and in every device.

In modern society the access to energy for large scale applications and handheld devices is essential for everyday life. The recent emphasis on renewable energy sources and electric vehicles has brought stricter requirements and a renewed interest in battery research. Due to intermittency of power delivered by solar or wind sources, an affordable energy storage solutions with a rapid charge and discharge rates are required. For transportation purposes energy storage must be both light and small with large storage capacities. These emerging and increasingly demanding applications are predicted to direct energy storage markets away from the traditional Lithium-Ion Battery (LIB) in the direction of new solutions as illustrated in Figure 10. Predictions indicate that by 2025, the majority of batteries sold will no longer be traditional LIB, and by 2032 the technology will be phased out completely from new products [3].
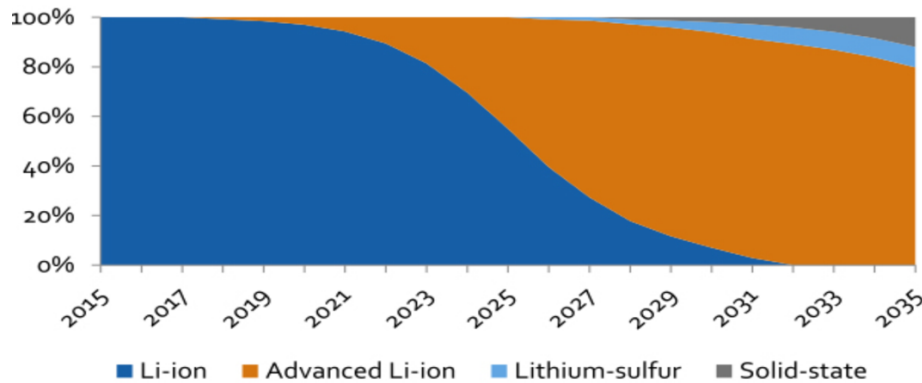
Figure 1: The figure illustrates the potential evolution of battery technologies. The graph shows the predicted transition from conventional LIBs to advanced versions based on the same chemical principles, and other technologies. The y-axis describes the percentage share of the battery market for transportation purposes and the x-axis is time in terms of year. An advanced LIB is here defined as "A varied mix of higher-voltage and higher-capacity materials" [3].

Another key issue which must be met is the development of a battery technology that relies on sustainable and abundant materials. Materials that may be extracted in a humane and manner than can be put to use at a low cost.

An improvement to the current Li-ion battery that has been researched extensively is replacing the carbon anode with silicon, improving the battery's ability to store energy in a weight- and volume-

efficient manner using an abundant and cheap material. Significant progress has been made addressing issues related to the silicon anode by nano-sized particles, carbon coating, doping, and various other methods. The solution of choice must be a realistic one, meaning it has to be applicable on a large-scale commercial level. This is true for both carbon coating and ball milling which therefore are solutions of great interest.

1.1   Aim of this Work

The aim of this work was to investigate two methods for enhancing the stability of silicon as an active material in anodes for lithium ion batteries. The first examined methods are ball milling and carbon coating procedures. The first step was to investigate the effect of ball milling on different types of silicon from a selection of different silicon sources. The results were then analyzed using BET analysis, SEM imaging and galvanostatic cycling to evaluate the effect on performance. Then, a procedure for carbon coating was tested and evaluated on a selected commercial silicon. SEM images were taken throughout the different coating stages and the resulting particles were cycled to examine the benefits of the carbon coating.

2 Theoretical Background

2.1 Introduction: An incremental zoom in

The following section contains the theoretical background necessary to appreciate the experimental work, results and related discussion in this thesis. The approach is a gradual zoom-in, starting with an introduction to common battery vocabulary before delving into LIB technology, its working principle and the key components. Special attention is paid to the formation of a Solid-Electrolyte Interphase (SEI) as this is important to the subject of the thesis. Then, the section focuses on the anode material and the possibility of using silicon, its advantages and disadvantages. These disadvantages may be mitigated through a number of methods described in the following section. The final section contains some theoretical considerations of a more practical nature related to the construction and performance testing of batteries.

2.2 Battery Vocabulary

In order to describe batteries in an efficient and precise manner some common vocabulary is required.

Specific capacity   The specific capacity is used in both a volumetric $[\text{mA h L}^{-1}]$ and gravimetric $[\text{mA h g}^{-1}]$ context. It describes the energy stored per unit mass or per volume of active material. Often, a theoretical specific capacity is calculated based on ion charges and atomic density for a known structure. This estimate is frequently significantly larger than the observed specific capacity.

Coulombic efficiency   The Coulombic Efficiency (CE) of a cell is defined as the percentage of charge spent during charging which is returned upon discharge. Commonly presented as in Equation 1:

$$CE = \frac{Q_{out}}{Q_{in}} * 100\% \tag{1}$$

Where Q_{out} is the total charge retrieved during discharge, Q_{in} is the total charge spent during charging and CE is the efficiency given as a percentage value.

C-rate   The Charge-rate (C-rate) of a battery describes the discharge rate relative to maximum capacity. A battery with a capacity of $1000\,\text{mA h}$ discharged at a C-rate of 1C would provide $1000\,\text{mA}$ for an hour, while at a C-rate of 2C the same battery would, in theory, provide $2000\,\text{mA}$ for half an hour. Batteries with large power capabilities retain their capacity when discharged at high C-rate, but commonly the stability and capacity of a battery is reduced with increased C-rate.

Reversible capacity   The reversible capacity of a cell is the capacity which the cell is able to retain for a given number of cycles. It is commonly determined by calculating an average capacity for a range of cycles excluding the initial cycles.

Irreversible/reversible capacity loss   Irreversible Capacity Loss (ICL) is the permanent decrease in the capacity of a battery, also known as capacity fade.

	Reversible Capacity Loss (RCL) loss is self-discharge and does not affect the capacity of the battery for cycles following the first cycle after the loss has occurred.
Cycle life	The cycle life of a battery is commonly defined as the number of cycles until the discharge energy of a cycle has reached 80% of initial capacity.
Anode Loading	The anode loading or simply the loading of an electrode is the amount of active material per unit area. Commonly given in units of $mg\,cm^{-2}$.
Solid Electrolyte Interphase	The SEI is a layer which forms at the boundary between the battery electrodes and the electrolyte. In most cases the formation of the SEI is detrimental to the battery performance. However, most batteries rely on the formation of a stable SEI which acts as a protective layer at the electrode surface preventing further SEI from forming.
Open Circuit Voltage	The Open Circuit Voltage (OCV) of a battery is the potential difference between the two electrodes when no current is flowing between them.

2.3 Lithium-Ion Battery

2.3.1 An Overview of Key Properties for Batteries Today

For the evaluation of battery technology, the criteria highlighted by the European Union (EU) are safety, performance and durability, sustainability, transport-ability and second use. These are then divided into sub-groups, some of which are capacity, power, cycling life, materials/resource efficiency and recyclability, all of which must be evaluated with respect to the cost [4]. The evolving requirements for batteries triggered increased battery research and causes the gradual transition from technology which is almost three decades old [5].

There are many possible battery technologies and some serve their specific niche in the commercial market. Batteries are divided into two subgroups based on their use. Primary batteries are discharged only once and are then no longer functional. Secondary batteries can be charged and discharged multiple times. Three of the common options for secondary batteries are lead-acid batteries, Nickel Metal Hydride (NiMH) batteries, and the LIB.

The lead-acid battery is primarily famous for its use as a car battery. However, in 2002 the lead-acid battery was the most widely used rechargeable battery in the world [6]. In 2016 the production of lead-acid batteries accounted for most of the value created in the secondary battery market. The major advantages of the technology are the low cost, high temperature stability, and excellent performance at high current densities. They are frequently used for grid applications and are becoming increasingly viable in terms of sustainability due to improved recyclability. The disadvantages are low volumetric- and gravimetric specific capacity, limited cycle life, and the high toxicity of the lead [7].

NiMH batteries utilize a metal hydride and a nickel hydroxide electrode with an alkaline electrolyte. They have been employed in hybrid vehicles and numerous portable electronic devices. They frequently employ a high content of expensive metals [8] and have a lower specific energy and are sensitive to storage at high temperatures. LIBs are expected to take over the hybrid electric vehicle market as they have a larger lifetime capacity and production of the constituents is less damaging for the environment [9].

The first batteries based on lithium ion transfer were introduced to the market in 1991 by Sony [10]. Initially, the technology was utilized for portable electronic devices and use has later expanded to electric vehicles. On a fundamental level the advantage of lithium for energy storage technology is the unique combination of the lowest reduction potential and lithium's small atomic size and weight [11]. LIBs therefore have the potential of high volumetric and gravimetric capacities. Both are key parameters for application in transport vehicles and portable electronics. Table 1 compares key properties of some common battery technologies.

Table 1: An overview of key properties for common battery technologies [12]. NiMH are frequently replaced by LIBs in modern devices. lead-acid batteries are frequently used for applications where there are few requirements beyond minimizing cost.

Battery Technology	Volumteric specific capacity $[Wh/l]$	Gravimetric specific capacity $[Wh/kg]$	Cost $[\$/kWh]$	Cycle life [number of cycles]
Li-ion	**150-200**	**100-200**	**800**	**<2500**
NiMH	200	40-60	500	>2500
Lead-acid	50-70	20-40	150	200

The Li-ion technology is more expensive than both NiMH and lead-acid batteries and it does not display the same cycling stability as NiMH. The application of the technology is therefore dependent

on the presence of additional requirements. In order to understand the properties of the LIB an investigation of the key components and working principles is required.

2.3.2 Working Principle

Secondary LIB are charged and discharged through reactions between lithium ions and its electrodes. During charging the lithium ions are stored the anode and the lithium ions are reduced. Correspondingly, the cathode is oxidized, which maintains the charge balance [13]. When the battery is discharged, the charge flow and the red-ox reaction is reversed. The anode is oxidized and the cathode is reduced. These processes are described by Equation 2 for the cathode, and Equation 3 for the anode. The overall battery reaction is given in Equation 4. As a result of these interactions, electrons move to and from the electrodes and a current is generated. The ions migrate between the electrodes through the electrolyte of choice.

$$\mathrm{LiMO_2} \underset{Discharge}{\overset{Charge}{\rightleftharpoons}} \mathrm{Li_{(1-x)}MO_2} + \mathrm{xLi^+} + \mathrm{xe^-} \tag{2}$$

$$\mathrm{C} + \mathrm{xLi^+} + \mathrm{xe^-} \underset{Discharge}{\overset{Charge}{\rightleftharpoons}} \mathrm{Li_xC} \tag{3}$$

$$\mathrm{LiMO_2} + \mathrm{C} \underset{Discharge}{\overset{Charge}{\rightleftharpoons}} \mathrm{Li_xC} + \mathrm{Li_{(1-x)}MO_2} \tag{4}$$
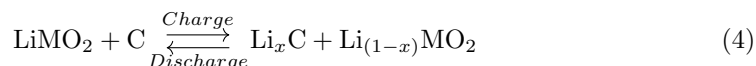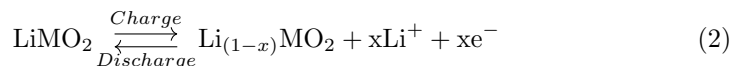
Here M is a metal cation and C is a carbon anode material. The movement of ions into or out of a solid material with a layered structure is known as intercalation and deintercalation, respectively. Often materials with layered structures are chosen as electrode materials. This structure facilitates the charging and discharging process and allows for an adequate C-rate due to the available pathways between layers. The open circuit voltage of a typical LIB is within the range of $3\,\mathrm{V}$ - $4\,\mathrm{V}$, depending on the electrode materials and other variables [14].

2.3.3 Key Components of LIBs

All conventional secondary battery technology consists of four main components which are essential for energy storage. The outline of a standard battery and its components are shown in Figure 2. These components are:

1. An electrode which acts as a cathode.

2. An electrode which acts as an anode.

3. An electrolyte which acts as a conductive medium.

4. A separator which creates a physical barrier between the electrodes.
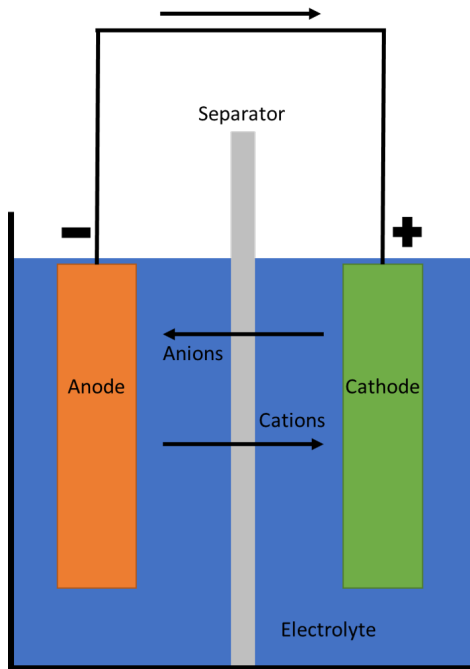
Figure 2: A simple sketch of the basic components in a battery. The arrows indicate the movement of ions and the direction of the generated electricity. The figure shows the battery during discharge.

Different electrode options may be classified in accordance with how they interact with ions during lithiation. The most widely commercialized electrodes are intercalation materials. These electrodes take advantage of the quick diffusion paths in structural voids in the atomic structure. They were first mainly layered structures, but recently spinels and other structures which also exhibit this behavior have become common. The other major group is the conversion materials. These materials are subject to a phase transformation during lithiation and this is often a barrier to use and a common topic of research [11].

The material and component cost is the most significant cost driver for LIBs. Other costs, such as assembly, only make up a small part of the batteries' total cost. However, the precise cost in $\frac{\$}{kWh}$ fluctuates significantly with electrode coating thickness and various other parameters [15].

The Cathode

The cathode is frequently a metal oxide, for instance lithium manganese oxide ($LiMn_2O_4$), or lithium cobalt oxide ($LiCoO_2$). These materials are chosen as they fulfill the requirements for cathode materials within an economically viable framework. Most crucial are the ability to store large amounts of lithium, high free energy of reaction for intercalation/deintercalation, high lithium ion diffusivity, and limited safety concerns. The cathode and the electrolyte can both contain lithium ions during battery assembly. These are the lithium ions which migrate and diffuse to store and generate electricity [13]. Increasing attention is being paid to the development of high voltage cathodes. For example, $LiMn_{1.5}Ni_{0.5}O_4$ (LMNO) batteries have been tested which exhibit a mean voltage of $4.75\,V$. This allows a larger energy density for the batteries [16].

The Anode

The initial commercialization of LIBs utilized lithium metal as an anode, but due to the instability of lithium it was later replaced by graphite. Graphite differs from lithium in terms of cycling behavior as the lithium has a changing structure and volume during lithiation. In fact the lithium tends to

grow dendrites during battery cycling. These can grow to physically connect the electrodes and short-circuiting the battery cell. Carbon does not change structure and has a limited volume increase of approximately 10% at full lithiation [17]. This enhancs stability and is ideal for battery electrodes. The theoretical specific capacity of graphite for LIB purposes is $372\,\mathrm{mA\,h\,g^{-1}}$ which is close to the commercialized capacity for graphite electrodes [18]. This capacity is reached when the carbon has stored one lithium ion for six atoms of carbon (LiC_6) [19].

Another commercialized anode material is Lithium Titanium Oxide (LTO) which has high thermal stability and cycle life [20]. It takes advantage of very small strains during cycling, allowing for formation of a SEI. One of the major drawbacks is the limited capacity of titanium, which limits the application. However, batteries with LTO-based anodes have become commercialized by the addition of Nb. These batteries have been commercialized by Toshiba and reached a capacity of $285\,\mathrm{mA\,g^{-1}}$ with a long life-time [21]. Another option is silicon, which is the second most abundant element in the earth's crust. It has been extensively researched as an alternate anode for LIBs. This will be addressed in Section 2.4.

The Electrolyte

The selection of an electrolyte depends on transport properties, electrochemical stability, temperature stability, and safety. The electrolyte commonly consists of a liquid solvent and a solute, typically an organic liquid with a dissolved salt. However, new options are emerging.

The most commonly applied alternative for LIB is an electrolyte composed of $LiPF_6$ and an organic solvent. $LiPF_6$ is a common solute as it has a high ionic conductivity and adequate safety properties. Another option is $LiClO_4$, but it is seldom commercialized due to its reactivity with solvents at high currents or temperatures [22]. Electrolytes with Lithium bis(fluorosulfonyl)imide (LiFSI) are currently being researched and has shown to exhibit improved electrolyte stability [23]. The most common solvents are typically carbonates, ethers and esters due to their high stability and compatibility with many relevant electrode materials. Common examples are Ethylene Carbonate (EC), Dimethyl Carbonate (DMC), and Propylene Carbonate (PC) [24].

To improve the behavior of the electrolyte a small amount of additives may be used. Vinylene Carbonate (VC) and phosphonate are are both additives which improve the stability of the solvent. Other additives such as N,N-diethylamino trimethyl-silane protect the cathode from acidic impurities and oxidation of the electrolyte solvents. Other additives stabilize the solute and improve safety parameters [25].

Recently, the field of solid-state electrolytes has been subject to large interest as they are more thermally stable than liquid electrolytes. This would significantly improve battery safety. In addition, an all-solid-state battery could have improved packing density and allow for the use of higher voltage cathodes as the solid-state electrolytes are more chemically stable. However, the conductivity of most viable candidates is still low and assuring contact between electrodes and electrolytes are currently preventing widespread application[26]. Some of the promising types are Sodium Super Ionic Conductor (NASICON), perovskite-structured and garnet-structured electrolytes [27].

Another emerging electrolyte option is the use of aqueous electrolytes. These are cheaper and safer than their organic counterparts, but there are concerns related to dissolution of electrodes in the water and the degradation of water during cycling [28].

The Separator

Battery cells contain a separator or diaphragm which allows for the migration of ions between the electrodes, but prevents physical contact. This prevents the battery from short-circuiting. Some separators have the added advantage of decomposing at increased temperatures which causes batteries to short circuit at an early stage during thermal runaway. This destroys the battery, but reduces the

risk of other harmful consequences as the short-circuiting of the cell stops heat generation. Common separator materials which exhibit this safety property are polyethylene and polypropylene [29].

2.3.4 Solid-Electrolyte Interphase Layer

The formation of an SEI layer occurs on most electrodes. It is the result of the reduction or oxidation potential of the electrode not corresponding to the stability window of the electrolyte. This results in the decomposition of the electrolyte, which deposits byproducts onto the electrode surface. The SEI layer therefore grows as long as surface potential remains outside the electrolyte stability window. However, the SEI layer is ionically conductive and thus allows migration of lithium ions. It forms a passivating film and results in a kinetically stable electrode while the cell remains unstable from a thermodynamic perspective. The ideal SEI has a high ionic conductivity while being dense and stable enough to prevent electron tunneling and thus prohibiting further electrolyte decomposition. The adverse effects of the formation of the layer are capacity fading, reduced power density and elevated resistance across the cell caused by consumption of lithium ions and electrolyte.

While the SEI forms on both the anode and the cathode, it is more disruptive on the anode due to the volume expansion of many anodes during lithiation. The exact composition of these SEI layers are difficult to determine as they appear to be complex layers of many different constituents with contributions both from lithium ions and decomposition products from the electrolyte. However, the different regions of the interphase are commonly divided into two zones. The section closest to the anode surface is an inorganic zone with components such as LiF, Li_2O and Li_2CO_3. Lithium cations are able to transport through this layer, but the electrolyte is not. The outer zone is made of a porous organic layer which also allows electrolyte to permeate through. It consists of a number of species such as Lithium ethylene glycol dicarbonate (LiEDC) and ROLi, where R is an organic group which depends on the specific electrolyte solute [30].

The choice of an electrolyte for a given battery system is essential to limit the adverse effects of the SEI formation. This requires that the salt and the solvent used are both compatible with the electrodes of choice.

2.4 Silicon anodes: Advantages & Disadvantages

One of the most successful and researched recent modifications to the traditional LIB has been the application of silicon as an anode material. Silicon has a specific capacity of $4200\,\mathrm{mA\,h\,g^{-1}}$ upon full lithiation ($Li_{22}Si_5$), but $3579\,\mathrm{mA\,h\,g^{-1}}$ ($Li_{15}Si_4$) has been suggested as a more likely structure at room temperature due to kinetic limitations[31], [32]. In terms of volumetric capacity this equates to roughly $8322\,\mathrm{mA\,h\,cm^{-3}}$[33]. In either case, this is a significant improvement of approximately an order of magnitude compared to graphite.

As a result of the lithiation process, the silicon undergoes structural changes and a volume expansion of approximately $300\,\%$ [34]. As the silicon is delithiated during discharge, the silicon contracts but does not return to its initial state. When the number of cycles increases the silicon gradually loses its morphology and is ultimately destroyed. The morphology change is illustrated in Figure 3.
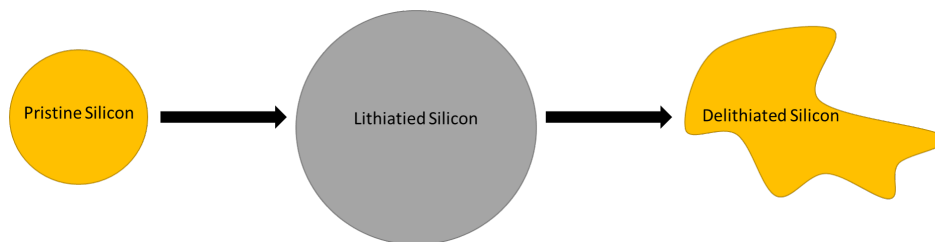
Figure 3: An illustration of the morphology change of silicon after delithiation.

To further examine the structural change occurring in silicon, an examination of a typical cyclic voltammogram from cycling the silicon is necessary, an example is given in Figure 4. By referencing the peaks in the voltammogram, the phase transitions may be identified. Peak 1 is the potential for initial transition from silicon to a $Li_{15}Si_4$ alloying phase. Peak 2 corresponds to a change to the fully lithiated state. The exact composition this phase is undetermined, but $Li_{22}Si_5$ has been suggested as a likely possibility[35]. The reverse transitions occur when the battery is delithiated. Peak 3 occurs when lithium ions are partially removed, forming a new phase of unknown composition Li_xSi_y. Peak 4 is the final stage and delithiated silicon is the resulting product. During the initial cycle, a small, additional peak is observed for the formation of a SEI-layer and a large peak due to the transition from crystalline silicon to an amorphous Li_xSi alloy structure [31].
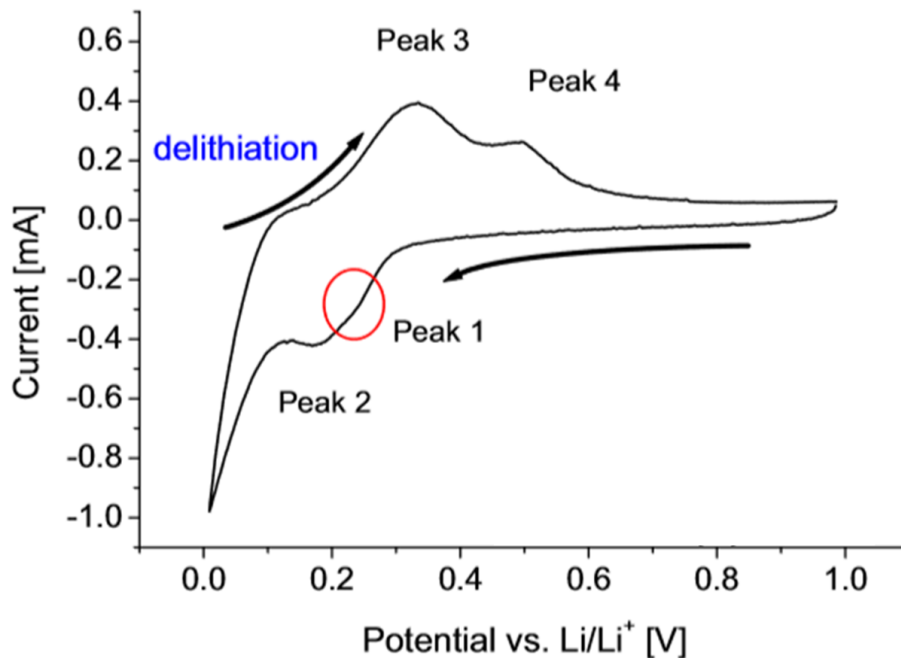
Figure 4: Cyclic voltammogram from cycling of a silicon rod anode. The graph shows the two main phase transitions during cycling. Figure adapted from [35].

During the initial discharge crystalline silicon is lithiated and an amorphous alloy phase (a-Li$_x$Si) is formed upon the first stage of lithiation of the structure. Simulations suggest that the transition point occurs at $x = 0.3$ [36]. Upon further lithiation, the amorphous alloy forms a crystalline structure at full lithiation (c-Li$_{15}$Si$_4$). *Ex situ* galvanostatic cycling studies suggest the formation of an over-lithiated phase if the voltage is allowed to reach 30 mV [37]. Thus, the cycling voltage is often limited to avoid this stage. When the battery is delithiated, it transitions from c-Li$_{3.75}$Si to a-Li$_{2.0}$Si and a-Li$_{1.1}$Si before reaching the fully delithiated state a-Si. Note that the silicon does not return to its initial crystalline state in the pure form, but remains in an amorphous state. Subsequent discharging follows a somewhat different pattern. The amorphous silicon is lithiated and transitions through peaks at a-Li$_{2.0}$Si and a-Li$_{3.5}$Si before the formation of a-Li$_{3.75}$Si which is then transformed to c-Li$_{3.75}$Si.

The phase transitions impact the voltage-current curve from cycling a battery cell as shown in Figure 4. Here each peak represents a change in the structure of the silicon.

(a)

(b)

(c)
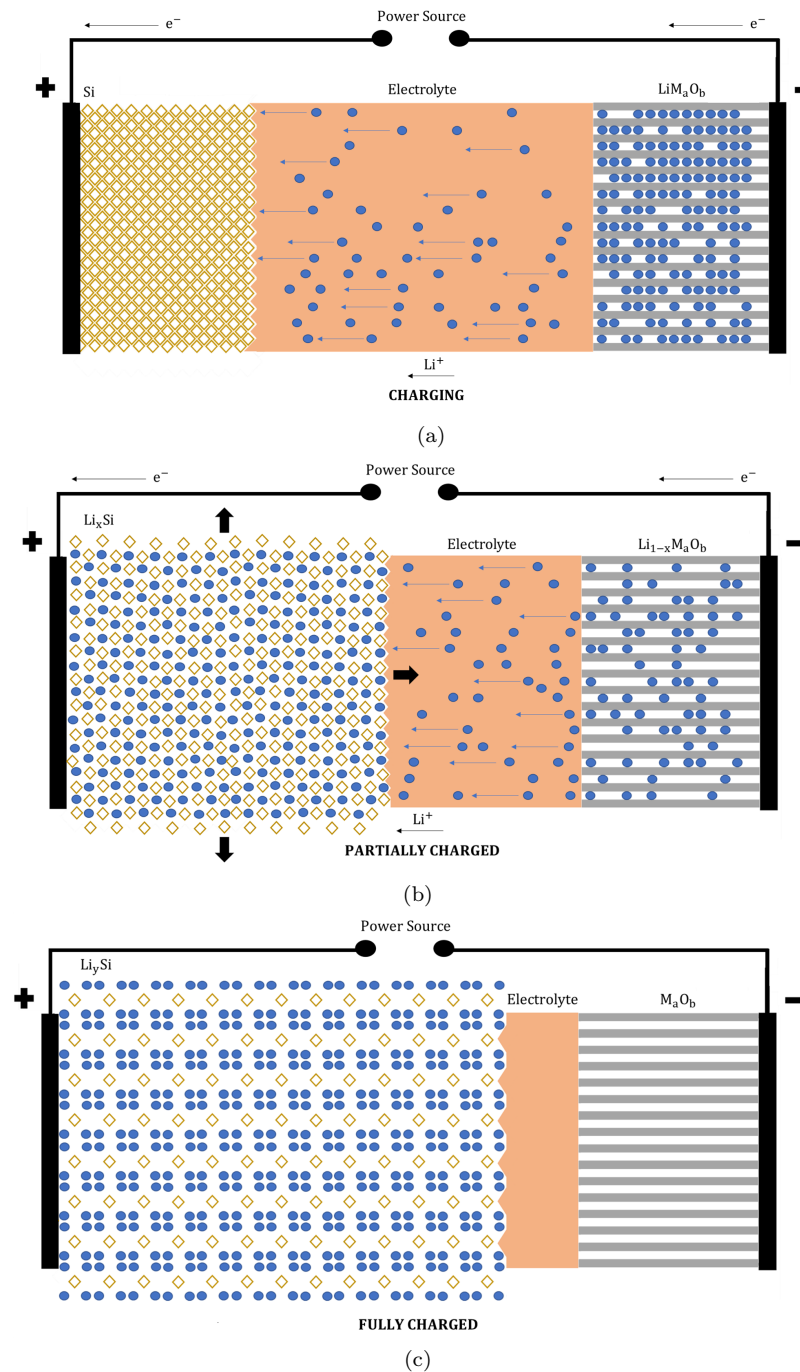
Figure 5: a) shows the initial charging of a LIB with a silicon anode. As a potential is applied, lithium ions migrate from the layered metal oxide to the silicon. Figure 4b) shows the expansion of the anode as the first lithium ions diffuse into the silicon changing the structure of the silicon. In figure 4c) the cell is considered fully charged and there are 4-5 lithium ions per silicon atom in the electrode. As the battery is discharged, the process is reversed and the silicon particles in the anode shrink to their initial size.

The problems arising as result of the volume change are excessive SEI formation and contact loss through fragmentation of particles or delamination.

Most significant of these challenges is the excessive SEI formation. This causes a lack of long term cycling stability, limiting use in a wide range of applications. Cycling of batteries cause formation of SEI as described in Section 2.3.4. When the battery is first charged, a SEI is established, consuming some of the lithium ions in the electrolyte and acts as an ionic insulator [38]. The consumption of lithium ions causes a high irreversible capacity loss during the first cycle, which may be identified through low CE. The SEI initially forms at the surface of silicon particles, but is not subject to the same volume change during cycling. Thus, the changing size of each particle causes partial disassembly of the SEI, exposing new areas of silicon to the electrolyte. New SEI forms at these exposed regions. This reoccurring process causes ongoing consumption of lithium ions which lowers the reversible energy capacity of the battery cell.

Another issue related to the volume change is contact loss. This occurs when the silicon particles during expansion/contraction lose contact with the current collector they are attached to, effectively reducing the amount of active material and lowering the reversible capacity. Contact loss may be caused by fragmentation of individual particles leading to small isolated silicon particles not in contact with the current collector, or due to detachment of entire silicon particles. In some cases larger parts the anode peels off from current collector causing loss electric contact in a process known as delamination.
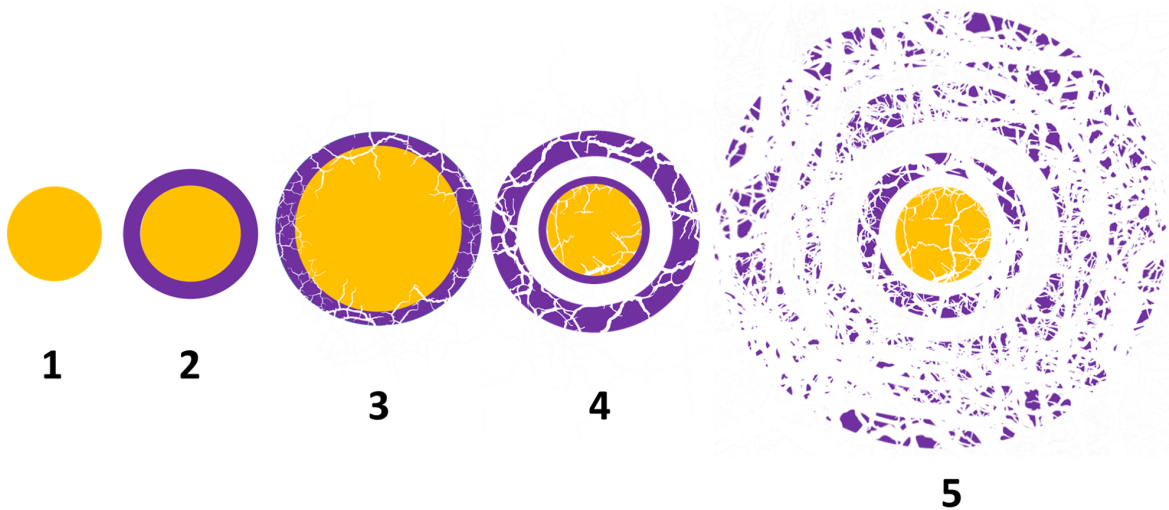
Figure 6: Shows the expansion and contraction cycle for a silicon particle during the charge and discharge cycles. Initially, a silicon-electrolyte interphase is established as lithiation begins. During lithiation, the particle expands and cracks due to internal stresses. The solid-electrolyte interface cracks due to the expansion of the particle. As the particle is delithiated, it shrinks back to initial size, leaving some of the solid-electrolyte interface in the electrolyte. In subsequent cycles new solid-electrolyte interface is established at the surface during charging. After many cycles, the repeated cracking has caused fragmentation of the particle and created much superfluous solid-electrolyte interface as illustrated.

Another challenge utilizing silicon as an anode is the inherent low conductivity of the silicon material [39]. This limits the cell's possible specific capacity at high C-rate.

These challenges have to varying degrees been addressed by various different techniques, some of which will be examined in Section 2.5.

Carbon coating is a procedure where a carbon layer is formed at the surface of silicon particles. These carbon-coated particles exhibit improved electrochemical properties [40]. This is mainly attributed to a combination of two positive effects. Firstly, by introducing a carbon coating with high conductivity relative to silicon, the overall conductivity is increased. This coating creates pathways for electrons to disperse into and out of the anode during charge and discharge, which lowers impedance and increases the possible C-rate of the cell. Secondly, research has indicated that the volume expansion of silicon during cycling is buffered by a carbon coating layer. This reduces the internal stress in the particle, lowering the probability of cracking and increasing stability. Carbon layers may hence serves as a buffer for the large volume increase during lithiation.

2.5 Methods for Improving the Performance of Silicon Anodes

2.5.1 Size, Morphology, and Loading

A requirement to make efficacious silicon anodes is to adjust the morphology and size of the silicon particles. The most significant single improvement to cycling stability of silicon anodes was the application of nanostructures. Varying structures have been researched for instance nano powders, nano rods and nanotubes. The small size of nano structures have been discovered to prevent fracture during lithiation and delithaition. The size limitation for fracture has been reported to be 150 nm. However, the surface area exposed to electrolyte increases as the particle size is reduced, resulting in more SEI formation and increased ICL [41].

As discussed in Section 2.4 the silicon anode structure is altered from crystalline to amorphous during cycling. Therefore, the use of amorphous silicon compared to the crystalline counterpart has been a topic of research. The desired advantages from applying amorphous silicon is reduced volume expansion and lower charge transfer resistance. The trade-off is lower electrical conductivity and reduced rate of lithium diffusion [42].

The loading of a cell has a significant effect on the stability and specific capacity of an electrode. Low loading electrodes and thin film electrodes frequently display high stability and specific capacity at large C-rate. This is likely due to a combination of two factors. Firstly, the thin film or low loading allows shorter diffusion distances for the lithium ions to reach the whole silicon anode. Secondly, the low loading results in mechanically less vulnerable systems which are less prone to fragmentation than their high loading counterpart. However, the large required area to get a significant energy storage per cell makes these solutions unrealistic for commercial applications.

2.5.2 Ball Milling

A common form of ball milling for silicon is planetary ball milling. Planetary ball milling is a procedure to adjust the Particle Size Distribution (PSD) and alter the morphology of silicon particles. Powder is locked in a chamber with larger balls as grinding media, and the chamber is rotated around its own axis while placed on sun wheel rotating in the opposite direction. These oppositely directed rotational movements induce forces in the chamber allowing for alteration of the particle morphology. The planetary ball mill is illustrated in Figure 8.

Horizontal section
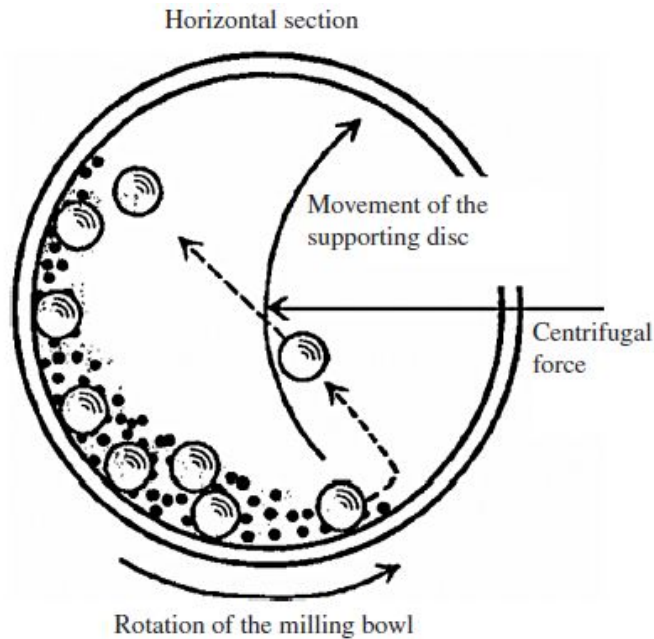
Figure 7: Illustration of the working principle of a planetary mill. The figure shows a horizontal cross-section of the milling bowl. The bowl is fastened to a supporting disc. The rotation of the milling bowl and the movement of the supporting disc is indicated with arrows. Arrows also indicate the resulting forces and the movement of the grinding balls. Small dots indicates the powder [43].

By ball milling coarse silicon particles, the resulting product is micrometric agglomerates with nanometric structures. Increased battery lifetime has been achieved by anodes made both by ball milling of pure silicon and by ball milling carbon along with silicon to create a silicon-carbon nanocomposite. To avoid oxidizing the silicon particles due to elevated temperature and exposure of new surfaces during ball milling, the process is carried out in an inert gas atmosphere, commonly argon. During the ball milling process, large particles are broken into smaller fragments which cold weld to larger agglomerates during repeated collisions.

Ball milled silicon has been shown to produce electrodes with lower initial and sustained ICL than silicon particles in the micrometer range. Research shows that the increase in stability is likely a result of reduced contact loss and SEI formation [33]. The reduction in contact loss is attributed to an increased amount of grain boundary regions which serve as facile diffusion pathways for lithium ions. This allows for a more homogeneous distribution of ions and a smoother phase transition with more gradual volume change and hence less cracking and contact loss. This also suggests a possible explanation for the similar formation of SEI despite the increased surface area of ball milled particles as less new surface area is created from each cycle. The effectiveness and effect of ball milling depends on the initial silicon morphology, ball-to-powder ratio, rotation speed, and the duration of the ball milling step. The difference in resulting PSD depending on the starting material is shown in Figure 8. The difference in results is explained by the fact that the ball milling effect relies on cold welding and fracturing, which both depend primarily on the mechanical properties of the material [33].
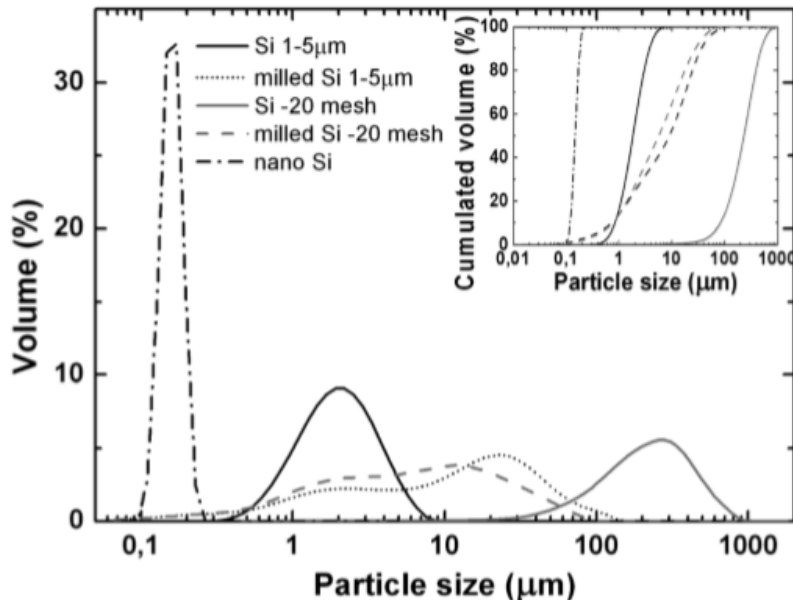
Figure 8: The graph shows the PSD of two different silicon powders before and after ball milling. Note that the PSD of the Si 1-5μm is shifted towards larger particles while the PSD of the Si-20 mesh moves towards smaller particles. Nano Si is shown in the graph for comparison. The inset shows the cumulative PSD for each of the five silicon types [33].

Besides the reduced cost of production, ball milled powder has several advantages compared to nano-metric silicon powders. The larger structures have reduced toxicity as the common safety concerns associated with powders in the nanometric size range is avoided. In addition, the ball milled structures have been reported to outperform the nanometric particles with respect to cycling stability. This has been suggested to be caused by the establishment of a better conductive network between larger structures. This network is created by the carbon black and graphite added to the electrode. If volumetric capacity is a key concern, this further favors the use of ball milled agglomerates because they display a tap density four times higher than their nanometric counterparts and thus an improved volumetric specific capacity[33].

2.5.3 Prelithiation

When an electrode of silicon is described as prelithiated, the lithium ions have been diffused into the silicon anode prior to the first charge/discharge cycle. The main advantage gained from prelithiation is mitigation of the irreversible capacity loss from the formation of an SEI during initial cycling. Due to the additional lithium ions in the silicon anode, there is an initial surplus of lithium ions in the cell. This reduces the SEI formation and thus the ICL. However, in the case of over-lithiation, a metallic lithium layer may form on the anode which may cause safety hazards due to the formation of dendrites. It is important to note that if the prelithiation process introduces a significant amount of non-lithium species to the anode, the gain in specific energy is reduced due to increased electrode mass.

Additional benefits of prelithiation to the performance of a silicon electrode have been investigated. Some research suggests that prelithiation reduces the impedance of the battery cell and reduces

cracking and pulverization from volume expansion. The latter is attributed to increase in volume during prelithiation which reduces relative volume changes from cycling[44]. It has been suggested that SEI with improved stability and formation properties may be designed at a prelithiation stage. However, this has yet to be sufficiently confirmed [45].

2.5.4 Doping and Alloying

A possible solution to the issue of low conductivity of Si is the introduction of additional charge carriers through p-type or n-type doping or alloying. By adding charge carriers to the electrode, an increase in conductivity and a decrease in impedance is expected. A common element for n-type doping is phosphorus, which has been reported to improve the performance of silicon anodes at low doping levels of 124 ppm [46]. Some results also suggest that the presence of small amounts of phosphorus may limit phase transformation during lithiation[46]. This would reduce the volume expansion of the anode and prolong battery cycling stability.Research on silicon nanowires suggest significant reversible specific capacity improvements after phosphorus doping [19]. However, other research suggests no significant improvements for substantial phosphorus alloying levels of 1.8 %at [47].

Different methods of phosphorus doping have been tested and both plasma arc discharge [48] and ball milling [49] have shown promising results in terms of successful introduction of phosphorus and increased anode performance.

2.5.5 Carbon Coating

Carbon coating is a procedure where a carbon layer is formed at the surface of silicon particles. These carbon-coated particles exhibit improved electrochemical properties [40]. This is mainly attributed to a combination of two positive effects. Firstly, by introducing a carbon coating with high conductivity relative to silicon, the overall conductivity is increased. This coating creates pathways for electrons to disperse into and out of the anode during charge and discharge, which lowers impedance and increases the possible C-rate of the cell. Secondly, research has indicated that the volume expansion of silicon during cycling is buffered by a carbon coating layer. This reduces the internal stress in the particle, lowering the probability of cracking and increasing stability. Carbon layers may also limit the formation of SEI formation as they restrict the contact between the anode surface and the electrolyte.

There are many variations on the carbon coating of silicon particles. For instance, yolk-shell structures which where there is a void space between the carbon shell and the particle, allowing for some expansion of the silicon[50]. Another example is thin graphene layers which act as a high conductivity grid while not reducing the specific capacity significantly [51]. These are just some examples of sophisticated coating structures attempted.

In order to benefit from the advantages of carbon coating, the coating is required to be within a limited thickness range. A layer that is too thin would break up during cycling and lose its beneficial properties. If the carbon layer is too thick, there is an increased risk of rupture due to a decrease in the coating's toughness. In addition, any gain in specific cycling capacity would diminish as the relative amount of carbon content increases due to its lower energy capacity relative to silicon. An adequately thick carbon coating may be established by different methods.

The Sugar Route

A possible method for carbon coating is the use of sucrose as an organic precursor. One possible way to do this is by dissolving the sucrose in $3wt\%$ H_2SO_4 and ultrasonicating at $50\,°C$ for an hour before heating to $95\,°C$ for an additional hour. Then the solution is dried at $150\,°C$. Carbonization is performed at $900\,°C$ for 5 hours with a constant Ar flow. This route has been proposed by Jaumann *et al.* [52]. Figure 14 shows a TEM image of the resulting layer.
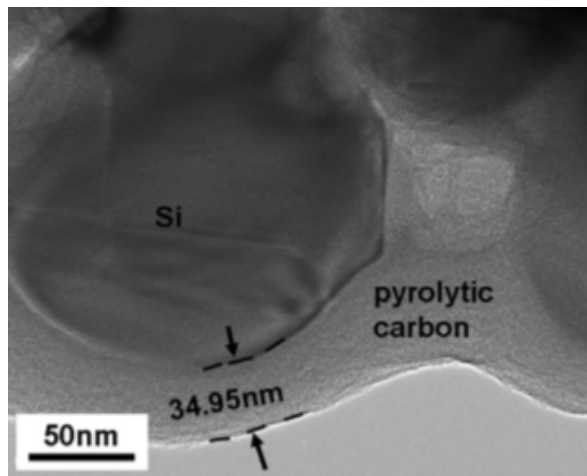
Figure 9: TEM image of a carbon coating layer created by Chen *et al.* using sucrose as a precursor for coating and pyrolysing the sample for $3\,h$ at $600\,°C$ [53]

Chen *et al.* [53] achieved a discharge capacity of $1215\,mA\,h\,g^{-1}$ at a current of $600\,mA\,g$ after 50 cycles. They used a similar procedure with pyrolysis at $600\,°C$ instead of carbonization.

The Phenolic Resin Route

Carbon coatings can also be synthesized using a phenolic resin by mixing melted phenol with formaldehyde in an aqueous solution. Other organic substances with a similar hydroxide functional group may also be utilized, for instance, resorcinol. The advantage using this route is the simplicity, scalability, and resulting potential for commercialization. In addition, the route is reliable as it is well known and researched. Catalyzed by the addition of a basic solution of sodium hydroxide, the phenol and formaldehyde react to form hydroxymethylphenol of various isomers. These products further react through polymerization or vaporization to form polymer chains. The solution is then neutralized by addition of hydrochloric acid before it is dried. This solution will eventually form the carbon coating layer. Separately, a suspension of silicon particles in ethanol is created. As the ethanol evaporates, the hydroxyl groups of the organic polymer form hydrogen bonds with the silicon dioxide formed at the particle surface. This establishes an organic coating during subsequent mixing. The coated particles are then dried and carbonized at a high temperature and a carbon shell is formed around each particle [2].
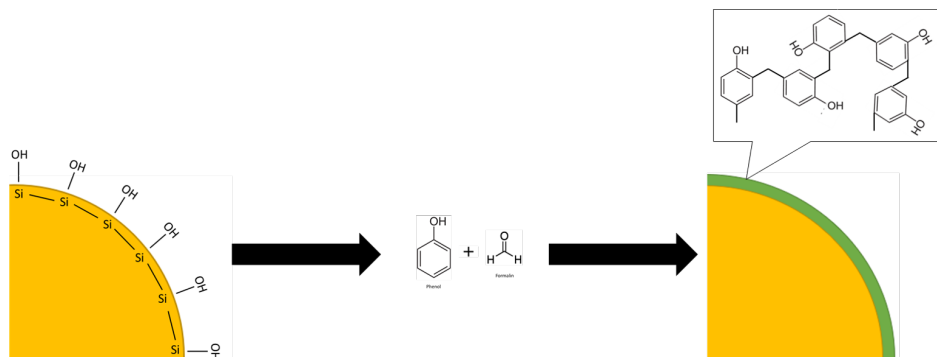
Figure 10: A figure illustrating the formation of a polymer from formaldehyde and phenol

A summary of the proposed reaction mechanisms from literature for the formation of a phenolic resin with formaldehyde as a cross-linker is given in Figure 11.
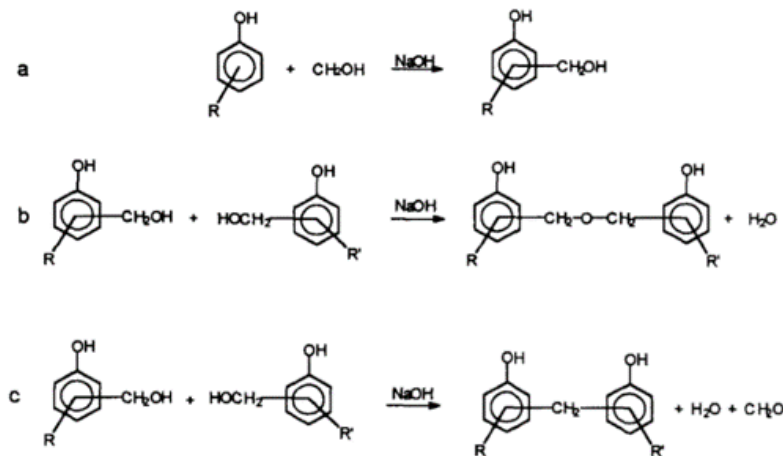
Figure 11: a) The initial condensation stage. b) and c) The proposed mechanism for further polymerization. b) dehydration with loss of water, c) dehydration with loss of formaldehyde and water [54]

2.6 Theoretical Remarks on Practical Matters

The following section contains some theoretical considerations when implementing the anode material into an actual cell and how to assess the performance. Moving closer to actual application of the material a number of additional factors must be taken into account.

2.6.1 Electrode Composition

When creating an anode slurry for a silicon anode, a mix of carbon and silicon along with a binder material is usually included in the slurry to achieve adequate performance. The large fraction of carbon in the anode reduces the theoretical capacity significantly, but combats the low conductivity and cycling stability of the silicon. To ensure contact with the current collector and a continuous anode structure which does not disintegrate upon cycling, a binder is essential.

The three binders conventionally used for LIB anodes are Polyvinylidene Diflouride (PVDF), Polyacrylic Acid (PAA), and Carboxymethyl Cellulose (CMC). Figure 12 show the chemical structure of these three common binders. PVDF has shown very poor cycling performance in silicon-carbon composite anodes. Even for low silicon content, the anode rapidly disintegrates and is reduced to capacity lower than the pure carbon counterpart. This is likely due to the stresses induced by the volume change of silicon breaking the carbon network apart due to two reasons. Firstly, the PVDF is unable to keep the particles connected. Secondly the contact loss of the silicon itself from the current collector [55].

PAA has shown significantly more promise in silicon-carbon composites. Its positive contribution has been proposed to be the result of a large amount of −COOH groups, which creates a mechanically-stable bonding as they form hydrogen bonds with the silicon oxide groups on the surface. The binder

has been suggested to outperform the other binders in part due to the formation of a superior SEI. Characterization of the interphase layer for PAA electrodes show an improved homogeneity of sulfide distribution, reducing SEI formation and increasing capacity retention[56].

CMC is a water-soluble cellulose derivative and a common binder material. The water solubility makes it easy to work with. In addition, CMC is also more environmentally friendly and it is less toxic than alternatives such as PVDF. The carboxyl group in CMC interacts strongly with the silicon dioxide surface, binding the slurry together and creating a conducting network of carbon, graphite and silicon. At the early stages of slurry mixing, they form hydrogen bonds which transition to covalent bonds after drying, ensuring a strong connection between binder and particles. The buffer solution is added to facilitate the binding process. It does so by stabilizing the mixture at a pH of approximately three which favors formation of the silicon hydroxide and carboxyl groups required for the covalent bonds.
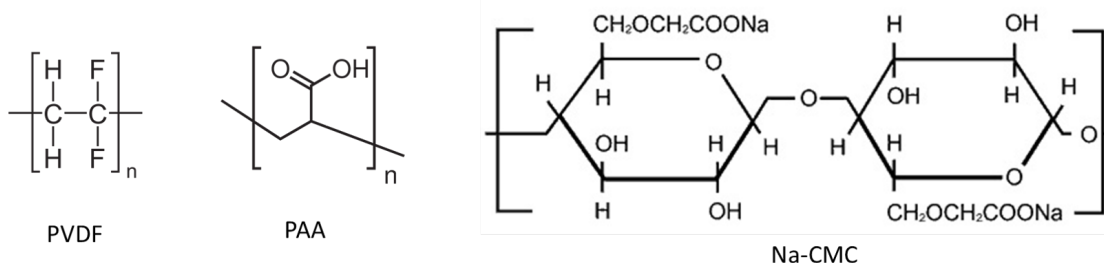
Figure 12: The chemical structure of the common binders for silicon composite anodes.

There are two forms of carbon added to the slurry mix. Graphite is added to enhance the conductivity of the anode and to act as a buffer for volume expansion of the silicon particles. In addition, amorphous carbon black is also added as a cheaper carbon source for the same purposes as graphite. Carbon black forms agglomerates with large void spaces which accommodates the expansion of silicon during lithiation. It is important to know the exact fraction of graphite, amorphous carbon and silicon in a cell in order to determine its theoretical capacity. This determines the current corresponding to a given C-rate during cell testing which is a crucial parameter when evaluating cycling stability.

2.6.2 Performance Testing of Anodes

Performance testing of a battery is done by repeatedly charging and discharging it and observing variations in key parameters such as initial energy capacity, coulombic efficiency and cycling stability. By evaluating the electrochemical data gathered during this procedure, it is possible to understand some of what is occurring during anode degradation.

When testing battery anodes, a half-cell is typically created. This half-cell is made to remove the cathode as a variable and isolate the performance of the anode as the performance-determining parameter. In order to do so, a lithium metal counter electrode is introduced. This serves as an unlimited source of lithium ions available when charging the battery. Hence, it is the ability of the anode to store lithium ions which limits the storage capacity. Figure 13 illustrates the key components of a coin half-cell for anode testing. The silicon anode is created on a Cu metal current collector and placed in a bottom cap of stainless steel. A separator membrane is placed on top of the anode with a plastic gasket on top. The gasket creates a small volume for the electrolyte and serves as a sealing mechanism for the cell. Electrolyte is added to the cell before a lithium counter electrode is inserted. Between the top cap and the counter electrode a spacer with a wave spring is placed. The spring introduces a

level of pressure to avoid void spaces within the cell and the spacer secures even distribution of this pressure over the electrodes' surface area.

Top cap (Stainless Steel)

Wave washer spring (Stainless Steel)

Spacer (Stainless Steel)

Lithium counter electrode

Electrolyte

Gasket

Separator

Silicon anode on copper current collector

Electrolyte

Bottom cap (Stainless Steel)
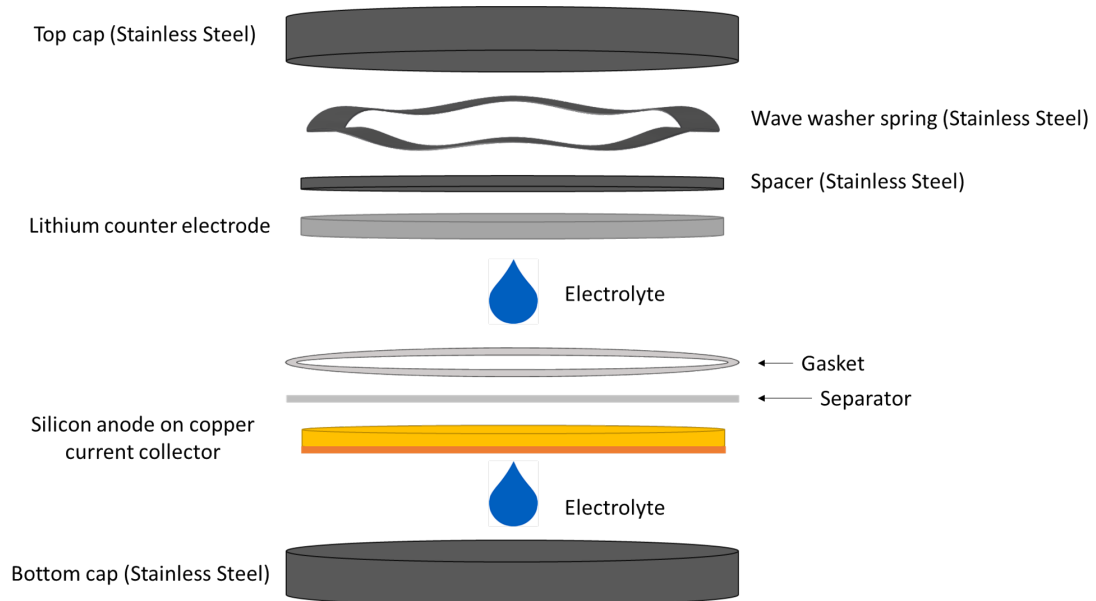
Figure 13: An illustration of the components in a typical half cell, which was also used for testing of silicon anodes in this research.

2.7 Characterization

2.7.1 Electrochemical Characterization

In order to evaluate the performance of an anode and the active material of choice in a battery cell, a number of electrochemical techniques may be used.

Galvanostatic Cycling

During galvanostatic cycling, the cell is charged and discharged continuously, emulating use in a battery. A constant current is applied to the cell and the resulting potential and cycle number is recorded. The desired current is calculated based on the theoretical capacity of the cell and given in terms of C-rate. During charging, charge is stored in the anode and during discharge, charge is extracted from the anode. Each cycle is typically limited by a cut-off voltage both during discharge and charge. When the potential reaches the cut-off voltage the cycling mode is switched to charging/discharging. The charge passed during a cycle is plotted against cycle number, allowing for the determination of ICL and thus cycling stability. A high ICL indicates either a large loss of lithium ions or a large increase in the resistance of the cell. By comparing the charge stored in the cell during charging with the charge extracted during discharge, the CE of the cell is determined. By dividing the charge capacity of a cycle with the mass of active material in the anode, the specific capacity of the active material is calculated. In some cases, a constant voltage step as the cell reaches cut-off voltage is introduced. This allows continued diffusion of lithium ions and reduces the effect of kinetic limitation. A few formation cycles at low C-rate is typically used to allow for the formation of a more stable SEI layer.

An additional plot which may be generated from galvanostatic cycling is the differential capacity plot. This is created by differentiating charge against the voltage change By plotting $\frac{dQ}{dV}$ against voltage, a differential capacity plot is created. This plot is used to analyze the phase transitions in the anode during cycling and is an important tool to analyze what is resulting in the observed capacity. The flat regions in the original voltage against capacity plots correspond to phase transitions in the anode material. These plateaus are observed as peaks in the differential capacity plot.

3 Experimental

3.1 Introduction: A Step-by-step Walk-through

The following experimental section contains a step-by-step walkthrough of the procedures performed to carbon coat silicon particles for use in battery anodes. The first section contains an overview of the samples created while each of the following sections describe a step in the experimental procedure. The experimental procedure for carbon coating is given as a flow chart in Section 8.3.

3.2 Sample Overview

For the investigation of ball milling properties of silicon four different silicon types were prepared in both pristine and ball milled conditions. The sample names, their characteristic particle sizes, and their structure types is given in Table 2.

Table 2: An overview of the tested silicon types, their structure and characteristic particle size.

Parameter	**Micro-Si**	**Nano-Si**	**Comm-Si**	**a-Si**
Structure	Crystalline	Crystalline	Crystalline	Amorphous
Particle size	1-5 µm	<100 nm	1-5 µm	<100 nm

For examining carbon coating procedure and the ideal polymer-to-carbon ratio, a number of samples with varying ratios were prepared. An overview of the samples and the corresponding Si:polymer mass ratio is given in Table 3. The polymer mix and method was adjusted with constant fractions of each reagent. The two reference samples are un-coated silicon that have also undergone carbonization to account for the structural change in the silicon during the carbonization stage. With the exception of Sample 1, each sample is from the same commercial silicon source and has been subjected to the same chemical coating procedure except for the Si:polymer mass ratio. The deviation related to this sample is explained in the coating section.

Table 3: An overview of the tested samples, the type of silicon and the polymer fraction of each sample. The notation "(BM)" indicates that these samples were ball milled as described is Section 3.3.

Sample Number	$\frac{Silicon}{Polymer}$
SP.5 (BM)	0.50
SP1.0 (BM)	1.00
SP1.37 (BM)	1.37
SP1.5 (BM)	1.50
SP2.0 (BM)	2.00
SP2.5 (BM)	2.50
SP3.0 (BM)	3.00
Reference (BM)	

3.3 Ball Milling

For the ball milling investigation the samples were prepared and ball-milled in an ambient atmosphere with balls of zirconia with a diameter of 3 mm. The ball mill used was a planetary ball mill of type

Fritsch Pulverisette 7 Micro Mill. A zirconia milling vial and lid with volume 80 mL was used as a container. For each sample 200 mg were ball milled with 5 g of balls, resulting in a ball-to-powder ratio of 25:1. The samples were ball-milled at 800 rpm for 20 min. The ball milling was performed in oxygen to allow for feasible commercialization.

For the carbon coating the same equipment was used, but ball milling was done in an argon atmosphere. The silicon was milled in batches of approximately 4 g at 800 rpm for 5 min with 100 g of balls, giving a ball-to-powder ratio of 25:1. The vial was filled with silicon powder and milling and sealed in an argon glove box with less than 0.1 ppm O_2 and H_2O to ensure an inert atmosphere during the process. The cap of the vial is tightened and then built up pressure is alleviated by adjusting the pressure valve. The vial was then removed from the glove box and ball milling was performed. After ball milling the vial was cooled back to room temperature after being heated during the process before being opened in air.

In both cases ball-milled silicon powder was gathered by gently shaking the zirconia balls while they were resting in a strainer and gently scraping the side of the vial.

Figure 14: a) The Fritsch Pulverisette 7 Micro Mill used for ball milling. b) An example of the type of milling vial used during ball milling.

3.4 Polymer Coating

The procedure was adopted from Meng *et al.* [1], for the creation of the resin, and Lu et al. [2] for the creation of a silicon suspension and coating procedure. The only significant change was mixing the phenol with the silicon particles prior to polymerization. This change provided a better chance to create a conformal carbon coating of the particles.

Phenol (Sigma-Aldrich, $\geq 99\%$) was melted at 42 °C (T_m). A suspension consisting of 500 mg silicon particles and 50 mL ethanol was prepared using an ultrasonic bath for 1 h. When the phenol was completely melted the suspension was poured into the container and allowed to cool to room temperature while stirring at 200 rpm for 4 hours. The stirring speed remained constant for the remainder of the process. Sodium hydroxide solution in water (20 %wt) was added to the mix over a period of 10 min. Then formaldehyde (Sigma-Aldrich, 37 %wt in H_2O) was added to the solution drop-wise and 25 mL of ethanol before heating at 70 °C for 1 hour. The basic solution was neutralized by slow addition of 0.6 mol L^{-1} hydrochloric acid. The solution was then heated to 77 °C, slowly evaporating ethanol and water without boiling. The resulting product was polymer coated silicon particles.

3.5 Carbonization

To carbonize the polymer layer, established in the coating step, each sample was heated in a tube furnace with an argon gas stream. The temperature was elevated to 820 °C, at a rate of 5 °C/ min, and kept constant for 2 h before cooling to room temperature. Due to the structural change of silicon during heat treatment the reference sample was also heated according to a similar heating profile.
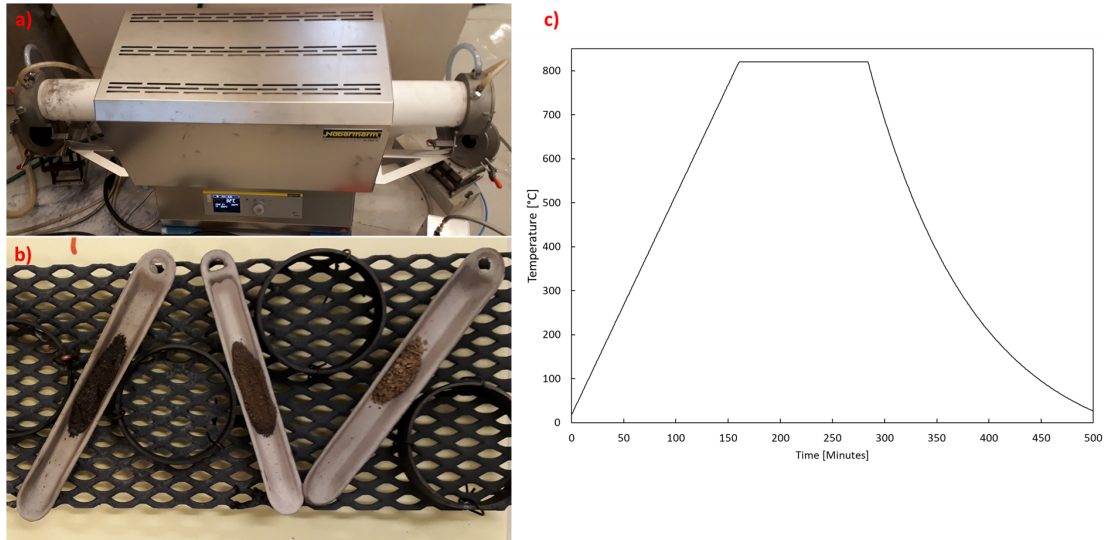
Figure 15: a) An image of the tube furnace used for carbonization. b) An image of the sample setup post carbonization. The polymer coated particles were held in ceramic crucibles during the process. c) The graph shows the heating profile used for carbonization. After carbonization the furnace was cooled to room temperature before the samples were extracted. The cooling part of the profile is a rough approximation as temperature was not recorded during cooling.

3.6 Anode Slurry

The components of the anode were mixed to a slurry and cast onto a dendritic copper foil. Na-CMC binder (15 mg), de-ionized water (0.4 mL), and a buffer solution of potassium hydroxide and citric acid (0.3 mL, pH of 2.87) were added to a vial and mixed in a Thinky mixer (ARE-250CE, Thinky Co). The mixing was performed in three identical stages, each mixing for 2 min with a rotation speed of 2000 rpm. After mixing the solution was visually inspected. If any particles were observed in the solution during inspection the mixing process was repeated. When the binder had been completely dissolved carbon black (15 mg, TIMCAL Super C65), graphite (10 mg, TIMCAL KS6L), and silicon (60 mg) were added. The vial was gently stirred and subjected to six cycles of ultrasonication using a ultrasonic mixer (Sonopuls HD2070, Bandelin Electronic) at 10 % power for 2 min. A list of the solid reagents and their corresponding wt% is given in Table 4. The main equipment used during the procedure is shown in Figure 16.

Table 4: An overview of the solid reagents for the anode slurry. The liquid added is evaporated as the anode is dried and not considered as a significant contributor to the final anode mass.

Reagents	Mass
CMC	15 wt%
Graphite	10 wt%
Carbon Black	15 wt%
Silicon	60 wt%
Total	**100 wt%**

The slurry was cast at a thickness of $76.2\,\mu m$ and an initial layer with mass of $550\,mg$ using a tape caster (MC20, Hohsen). The following layers each had approximately $150\,mg$ until all the slurry had been used. A dendritic copper foil (SE-Cu58, Schlenk) with a thickness of $18\,\mu m$ was used as substrate. The dendrites were oriented in parallel with the casting direction. The slurry was rested for approximately $30\,sec$ between each layer during casting.

After resting for at least 24 hours in open air at room temperature the slurries were dried in an Opsen Vacuum Oven at $120\,°C$ for $180\,min$. The cells were punched into $15\,mm$ in diameter discs and weighed in order to determine the loading of active material and calculate the current corresponding to the desired C-rate for battery testing.
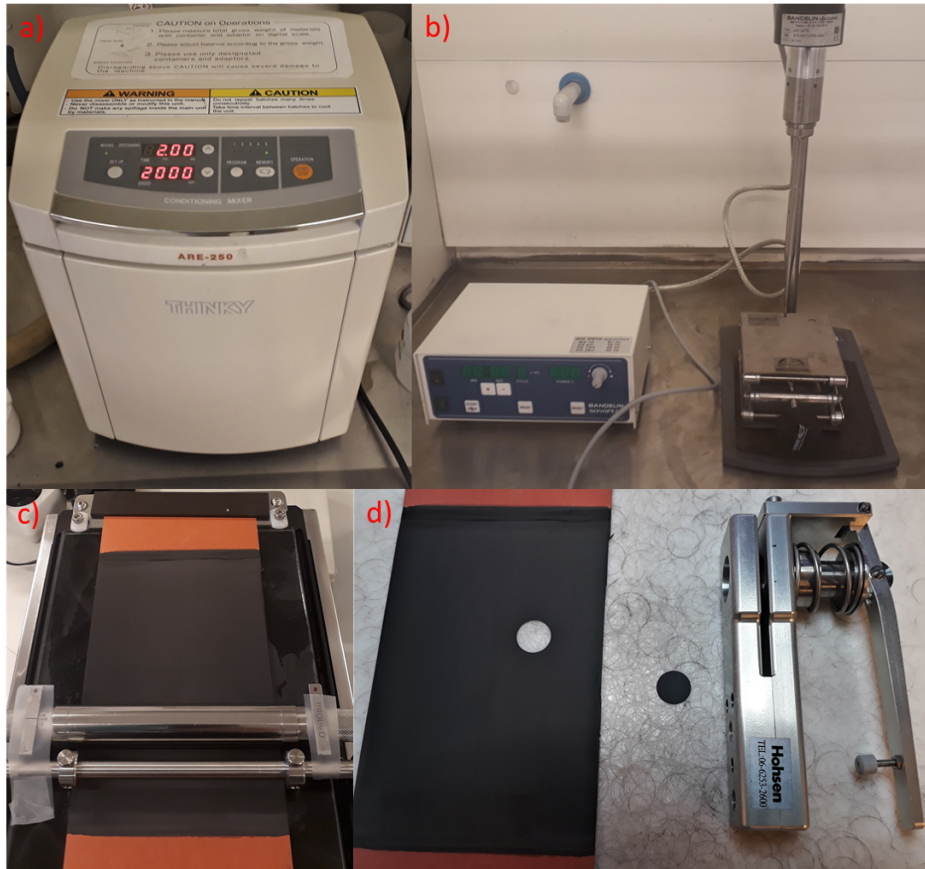
Figure 16: a) An image of the Thinky mixer used in the initial mixing of binder, buffer and deionized water. b) The ultrasonication stick used for the second mixing stage. The stick is inserted 0.5 cm -1 cm into the liquid during ultrasonication. c) The tape caster used for casting the slurry onto the dendritic copper foil. The doctor blade is used to adjust the casting thickness. d) The dried slurry on a copper foil, a punched cell and the cell puncher.

3.7 Coin Cell Assembly

The half cells were assembled in a coin cell format in an argon filled glove box (MBraun) with less than 0.1 ppm O_2 and H_2O to ensure an inert atmosphere during the process. A lithium metal cathode (99.99 %, LinYi Gelon LIB Co, 15 mm in diameter and 250 µm) was prepared by gently removing the surface layer using a scalpel. A single 18 mm in diameter separator (2400 Celgard, 25 µm thick) and S1 35 µL electrolyte were used. The electrolyte was distributed with 20 µL after placing the anode, and 15 µL between the separator and the lithium cathode after inserting a gasket. The electrolyte was a custom mix from Solvionics with 1.2 M in a 3-to-7 ethylene carbonate to ethyl methyl carbonate solution. Additives were 10 wt% fluoroethylene carbonate and 2 wt% vinylene carbonate. A single drop of electrolyte was placed in the coin cell bottom before inserting the anode, ensuring contact between the anode and the bottom cap and making it simpler to center the anode. The cell was sealed using a coin cell crimper (Hohsen) and removed from the glove box before washing with ethanol, labeling and drying. The make-up of the cell is illustrated in Figure 17.
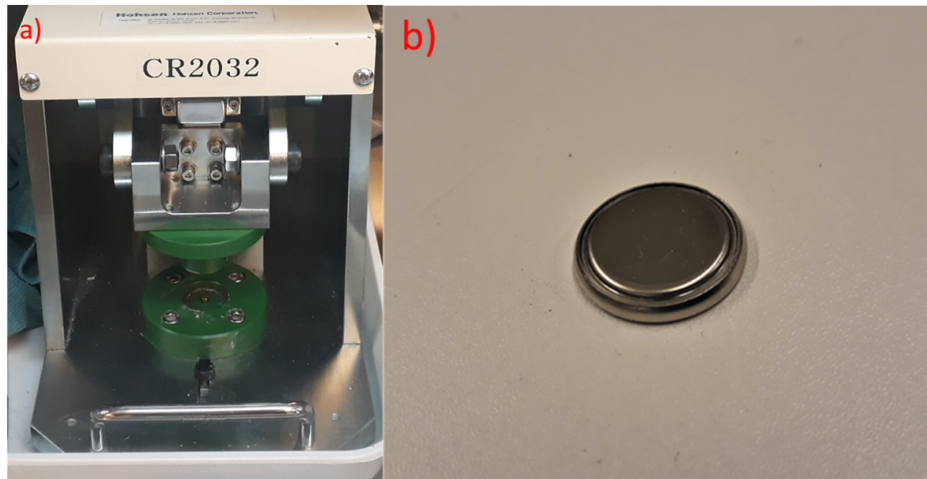
Figure 17: a) The coin cell crimper used to seal the coin cells after fabrication. The cell is placed at the center and pressure is applied until the metal is crimped. b) The finished coin cell.

3.8 Battery Testing

All of the batteries with were tested by repeated charge-discharge cycles in a battery tester (ARBIN BT-2000) as in Figure 18 from $50\,\mathrm{mV}$ to $1\,\mathrm{V}$. The cells for the ball milling investigation were cycled with three formation cycles at $\frac{C}{20}$ before a resting stage at OCV, followed by continuous cycling at $\frac{C}{10}$. Some of the batteries with carbon coated Si were rate tested by cycling five times at C-rate of $\frac{C}{20}$, $\frac{C}{10}$, $\frac{C}{5}$, $\frac{C}{2}$, $1C$, and $\frac{C}{20}$ again. The remaining cells were tested by cycling three formation cycles at $\frac{C}{20}$ before a resting stage at OCV. Then the rest of the batteries with carbon coated Si were cycled towards a maximum of 100 cycles at $\frac{C}{5}$ or the end of the project's timeframe.
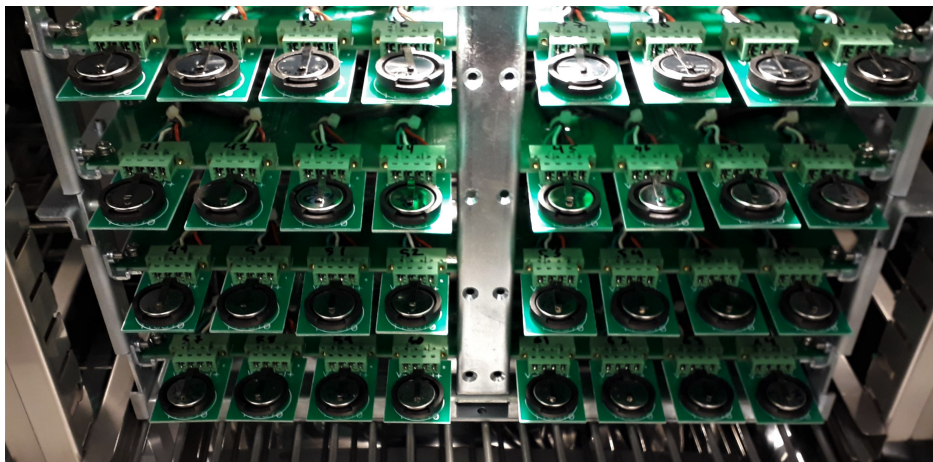
Figure 18: The cell tester. Each cell is inserted into a testing channel where it is charged and discharged. The testing channels are in a cabinet to control the temperature.

4 Results

The following section contains a summary of the results. It is split into two main sections. The first contains a summary of the ball milling investigation including Scanning Electron Microscopy (SEM) imaging, galvanostatic cycling data and Brunauer-Emmett-Teller (BET) surface area analysis. The section contains a summary of the coating investigation including SEM imaging, Scanning Transmission Electron Microscopy (STEM) imaging, galvanostatic cycling data, and rate testing.

4.1 Ball Milling Investigation

Results from the ball milling investigation are given in the following section.

4.1.1 Galvanostatic Cycling and BET investigation

The data presented in this section has been published as part of an article by Lai *et al.* [57].

Figure 19 shows the specific discharge capacity from cycling the different Si-types up to 200 cycles according to the description in Section 3.8. All batteries display a similar and expected gradual decrease in discharge capacity. The anodes with ball milled Si are outperformed by their pristine counterparts in all four cases, but in the case of a-Si the decline is much more severe than the rest of the samples. Some key values are summarized in Table 5.
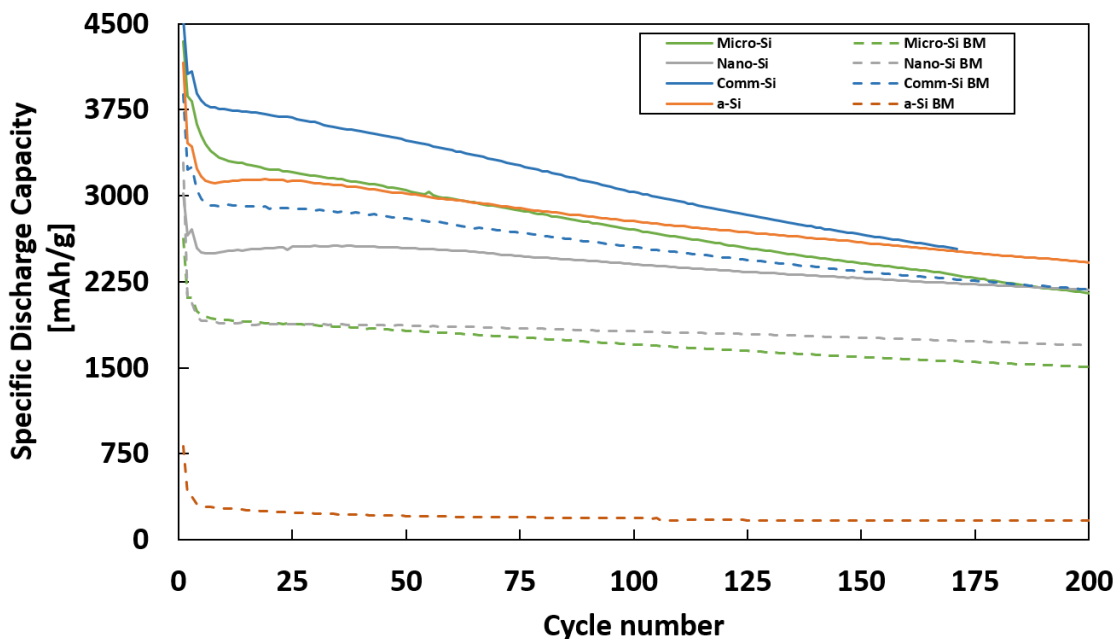
Figure 19: The graph shows the specific discharge capacity of different types of Si in pristine and ball milled condition.

Table 5: Some key values from battery cycling of each of the tested samples.

Si Type	Dis.capac [mAh/g]	Dis.capac [mAh/g]	Dis.capac [mAh/g]	Capacity Retention [%]
Cycle	1	20	150	150
Micro-Si	4348	3231	2411	55.45
Micro-Si BM	2630	1890	1594	60.60
Nano-Si	3021	2543	2280	75.47
Nano-Si BM	3288	1883	1763	53.61
Comm-Si	4550	3705	2659	58.44
Comm-Si BM	3882	2888	2340	60.27
a-Si	4161	3142	2592	62.29
a-Si BM	811	247	170	20.96

Figure 20 shows the first cycle CE for all Si-types along the primary vertical axis and the BET surface area along the secondary vertical axis. For all samples the CE is reduced after ball milling. The change is most significant in the case of a-Si. Each sample, with the exception of comm-Si shows an increased surface area after ball milling, the increase is most significant for a-Si. The BET data is given in Table 6.
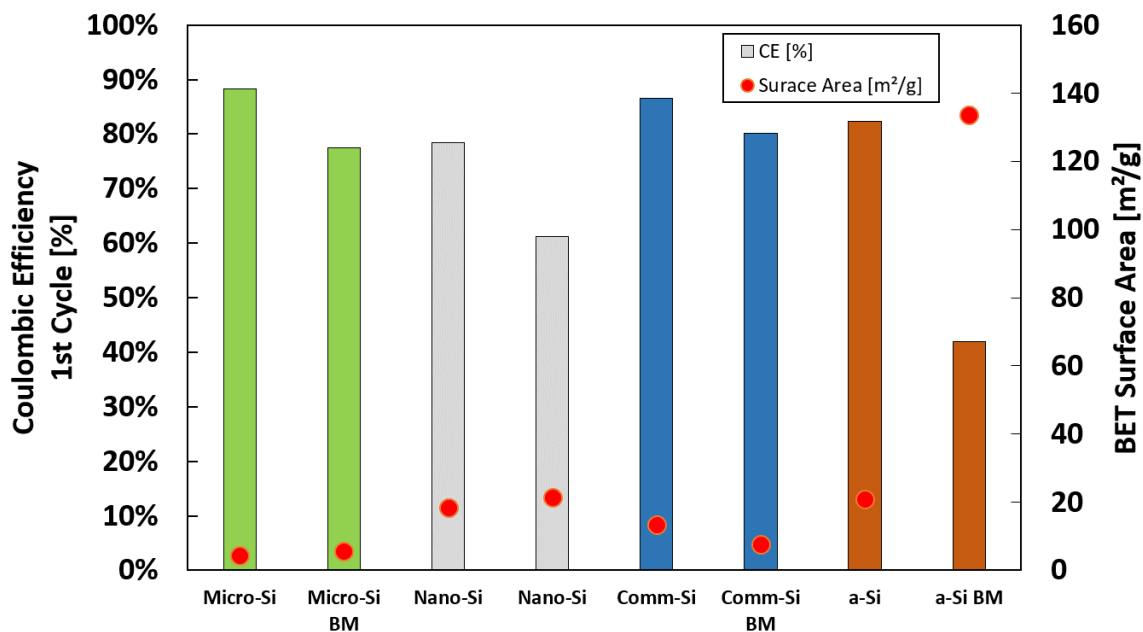
Figure 20: Coulombic efficiency for the first cycle of the cycling shown in Figure 19 for each type of Si is given on the primary vertical axis. The BET surface area is given on the secondary vertical axis.

Table 6: The result of BET analysis of the different types of Si.

Parameter	Micro-Si	Micro-Si BM	Nano-Si	Nano-Si BM	Comm-Si	Comm-Si BM	a-Si	a-Si BM
Surface area $[\mathrm{m}^2\,\mathrm{g}^{-1}]$	4.45	5.53	18.35	21.41	13.39	7.69	20.87	133.63
Pore size [Å]	120.38	139.50	90.00	142.20	187.92	143.31	126.92	60.03

4.2 Carbon Coating Investigation

4.2.1 SEM images

All the following images have been captured using a Hitachi S-4800 electron microscope. Samples were prepared by being dispersed in ethanol, ultrasonicated, and pipetted onto TEM grids and dried before imaging.

From pristine to ball milled particles

The first stage of the process was to ball mill the silicon particles. Figure 21 shows the silicon particles prior to any treatment. Figure 22 shows the resulting particles after ball milling according to the procedure described in Section 3.3. The particles had a wide range of different morphology, size and surface structure. The four particles are chosen to display this wide range and thus create a representation of the particle prior to ball milling. As seen, large flat and clean surfaces are observed. Long crack surfaces can be seen at the edges of particles.
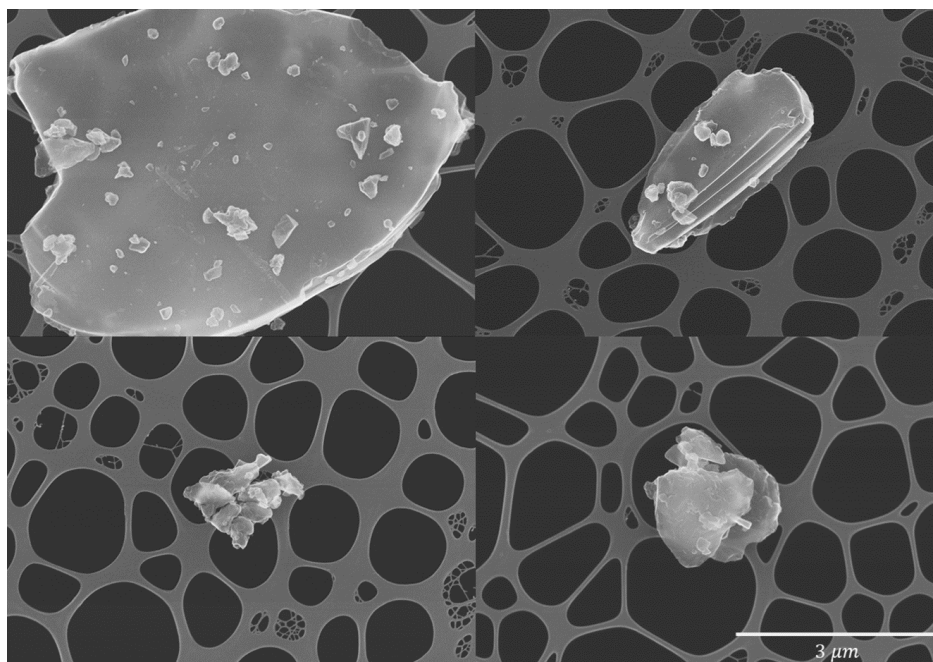
Figure 21: SEM images of the commercial Si used for battery anodes. An accelerating voltage of 30 kV and a working distance of 6 mm were used for imaging.

The particles after ball milling exhibit a rounded shape and limited large flat surfaces. The long cracking lines are no longer present. Each particles appears more like an agglomerate with an increased number of smaller particles attached to the surface.
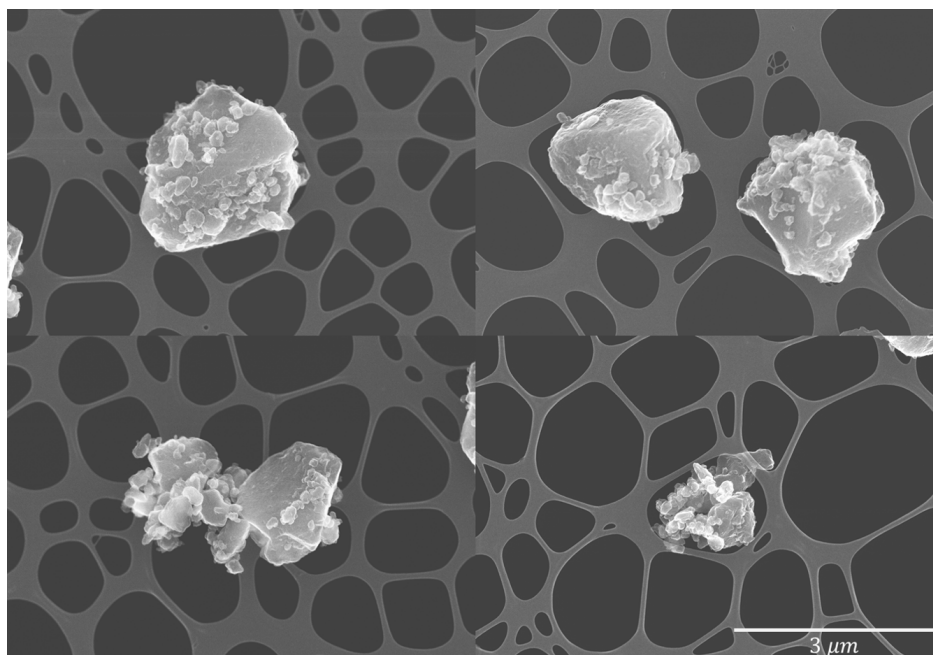
Figure 22: SEM images of the commercial Si used for battery anodes after ball milling. An accelerating voltage of $30\,kV$ and a working distance of $6\,mm$ were used for imaging.

Polymer coated particles

Particles were coated with varying amounts of phenol monomer and imaged in an attempt to observe polymer on the particles. This data was used continuously to evaluate the success of the polymer coating stage. The following images illustrate some of the varying results observed which are relevant for the subsequent discussion.

Figure 23 shows the first time an indication that the polymer was binding to the silicon surface. This was prior to implementing ball milling of the silicon particles. Figure 23 a) shows a pristine commercial Si particle with what appears like a polymer layer on the surface. Figure 23 b) is a STEM image of the same particle as in a), it reveals what appears to be a porous layer at the edges of the particle.
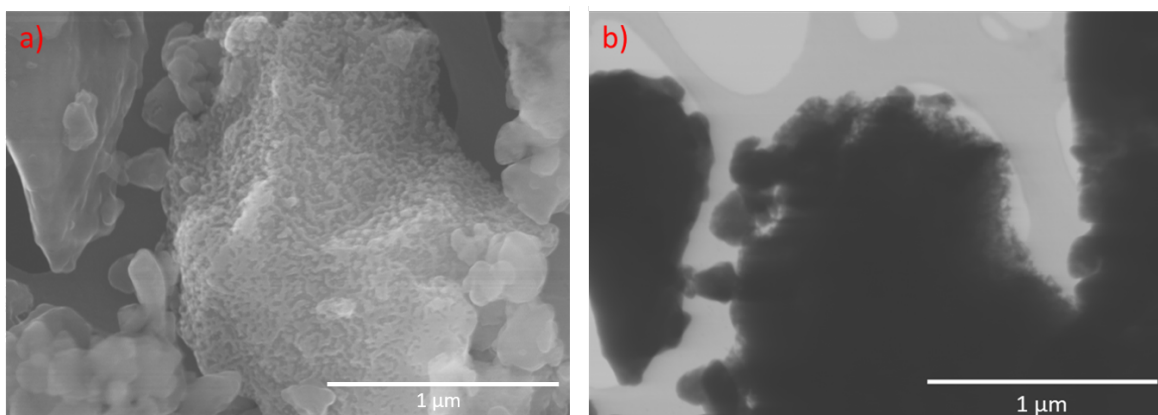
Figure 23: An accelerating voltage of $30\,kV$ and a working distance of $6\,mm$ were used for imaging.

Figure 24 shows the resulting difference between (a) SP0.5 and (b) SP1.37. The resulting particles and polymer mix display very different appearances. Figure 24 a) Is a SEM image of ball milled commercial Si in what appears to be large agglomerates bound together by polymer. Figure 24 b),here the particles do not agglomerate, but many spherical objects are observed.
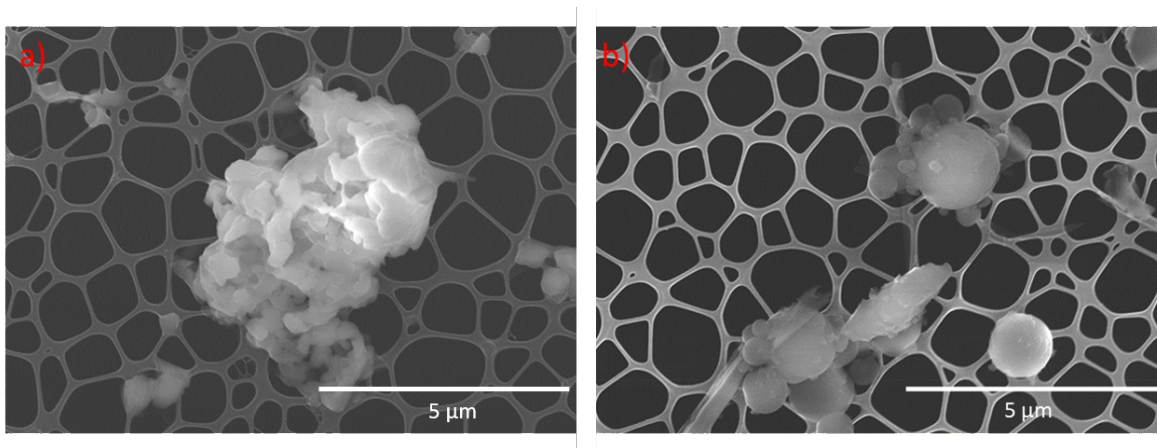
Figure 24: a) An accelerating voltage of 10 kV and a working distance of 6 mm were used for imaging. b) An accelerating voltage of 30 kV and a working distance of 6 mm were used for imaging.

Some of the particles with lower monomer-to-silicon ratio show little or no evidence of polymer coating visible within the resolution limits of the SEM, as illustrated in Figure 25. Figure 25 a) SEM image of ball milled commercial Si particles from SP3.0. If any polymer layer is present it appears indistinguishable from the regular silicon surface observed in Figure 22. Figure 25 b) is a SEM image of silicon particles from SP2.5. The image in Figure 25 b) appears very similar to Figure 25 a).
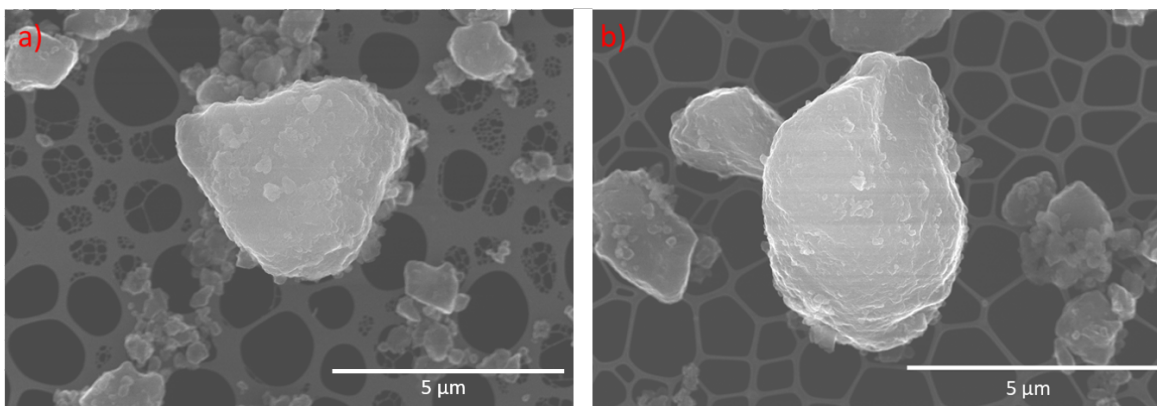
Figure 25: An accelerating voltage of 30 kV and a working distance of 6 mm were used for imaging.

Carbon coated particles

After carbonization as described in Section 3.5, the polymer layer has been carbonized and altered to a carbon coating. While difficult to see, with low monomer ratios, some evidence suggests that the particles may be coated.

Figure 26 shows the ball milled reference sample post carbonization. As the carbonization causes

a structural change in the silicon this image provides relevant comparison for surface structure and morphology changes due to carbonization between non coated and coated particles. Comparing Figure 26 with Figure 21 the surfaces and morphology displays no significant visible change.
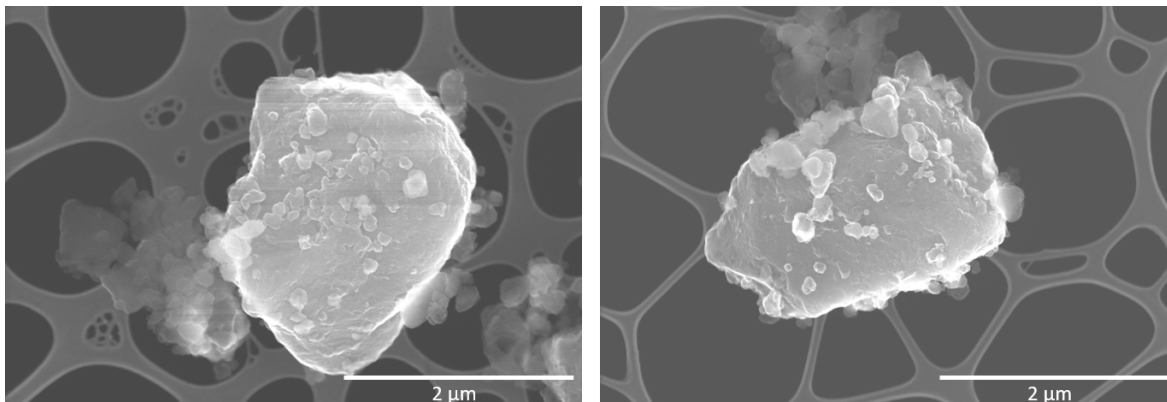
Figure 26: An accelerating voltage of 30 kV and a working distance of 6 mm were used.

As for the polymer coated particles different observations were made for high monomer content samples, Figure 27, and low monomer content samples, Figure 28.

Figure 27 a) and b) shows two examples of structures from SP1.37. The high polymer content appears to result in particle agglomerates as in Figure 27 a) and larger structures with flimsy edges and altered surface structure (b). For all these images it is problematic to distinguish effectively between carbon and silicon and determining the silicon content of the larger structures. The spherical shapes observed prior to carbonization are still present. However, they no longer exhibit the smooth surfaces. Figure 27 c) and d) shows two examples of structures from SP1.0. This sample contains a larger amount of polymer than SP1.37, but does not result in the same morphology. These particles do not form what appears to be a continuous surface as in Figure 27 b), but rather large agglomerates of distinctly different particles. This is most evident in Figure 27 d).
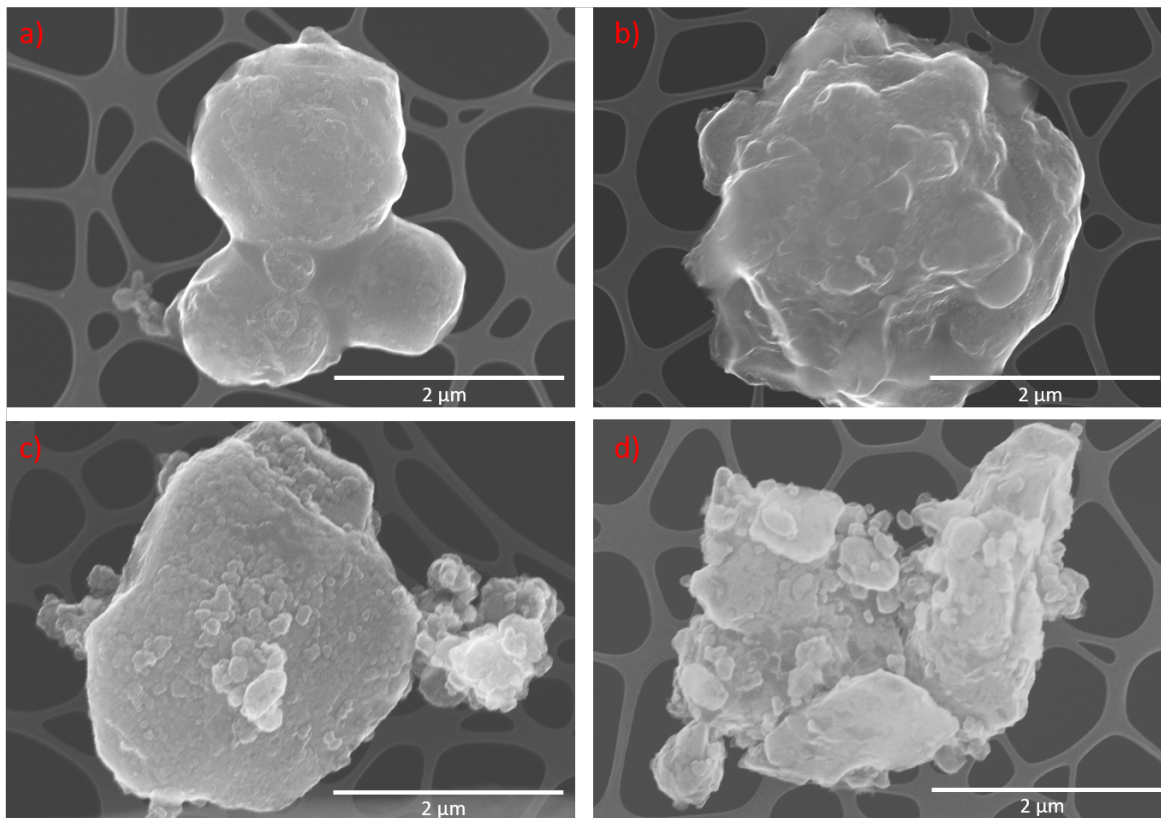
Figure 27: An accelerating voltage of 30 kV were used for all images. a) and b) were taken with a working distance of 9 mm. A working distance of 9 mm were used for c) and d).

Figure 28 shows particle agglomerates from a) SP2.0 and b) SP1.5. Large agglomerates are also formed at this polymer amount. However, the structure appears more complex as there are more observable small fragments at the surface of the agglomerates. This is most evident in Figure 28 a).
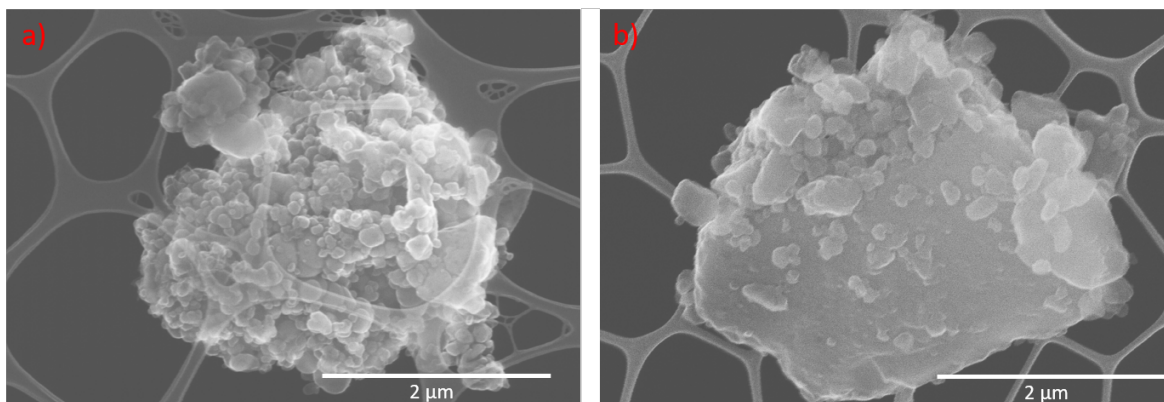
Figure 28: An accelerating voltage of 30 kV and a working distance of 9 mm were used for imaging.

4.2.2 Galvanostatic Cycling

Galvanostatic cycling of a selection of samples is shown in Figure 29. Each sample had a different Si:polymer ratio. The specific capacities are calculated based on the active material resulting from the loading mass of each cell and the slurry recipe given in Table 4. A total overview of galvanostatic cycling data is given in Section 8.4. The highest specific discharge capacity is observed for the Reference sample. The rest of the samples appear to decrease in capacity with increasing polymer content with the exception of SP1.0 which displays a higher discharge capacity than SP1.37 and a slightly higher discharge capacity than SP2.0. Sample 4 shows a rapidly declining capacity which stabilizes at $119.9 \, \mathrm{mA \, h \, g^{-1}}$ after the 5th cycle. All samples appear stable for the first 30 cycles, however differences in the ICL and the resulting capacity retention is observed. Table 7 contains a summary of key values.
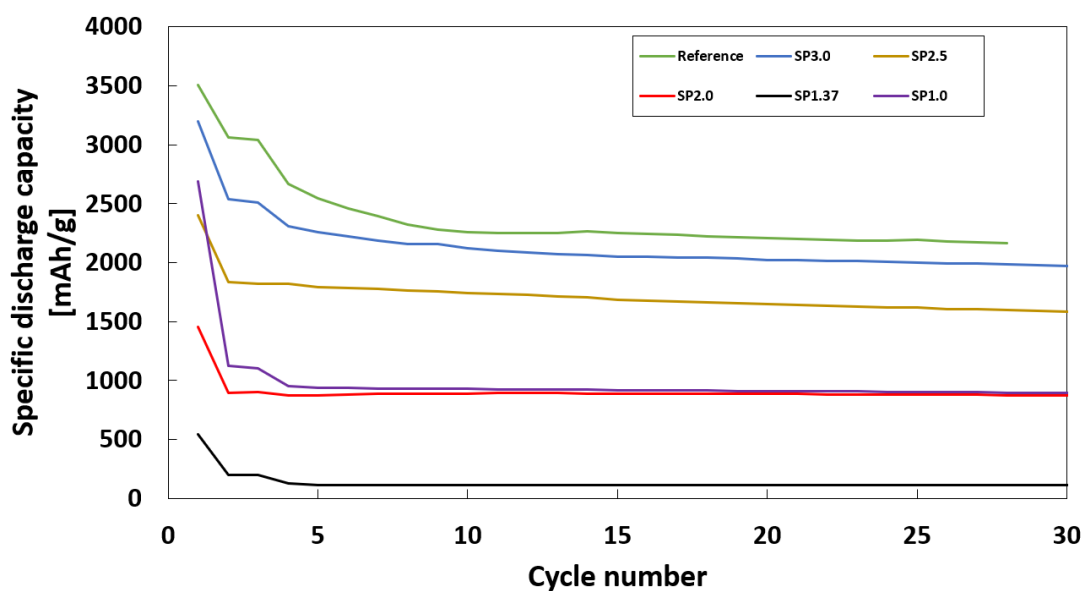
Figure 29: A plot of the galvanostatic cycling of a selection the samples. Specific discharge capacity is plotted against cycling number. The cycling was performed as described in Section 3.8. Si:polymer ratio is given as a parenthesis in the legend.

Table 7: Some key values from battery cycling for each of the tested samples.

Si Type	Dis.capac [mAh/g]	Dis.capac [mAh/g]	Capacity Retention [%]
Cycle	1	25	25
Reference	3505	2190	62.48
SP3.0	3201	2002	62.54
SP2.5	2398	1616	67.39
SP2.0	1458	881	60.42
SP1.37	544	115	21.14
SP1.0	2685	903	33.63

The CE for all samples were calculated as described in Section 2.2 and is given in Figure 30. After initially noisy measurements the samples stabilize at a value close to 100 %. The exception is SP2.5 which stabilizes at a low CE of 94%, indicating a high ICL.
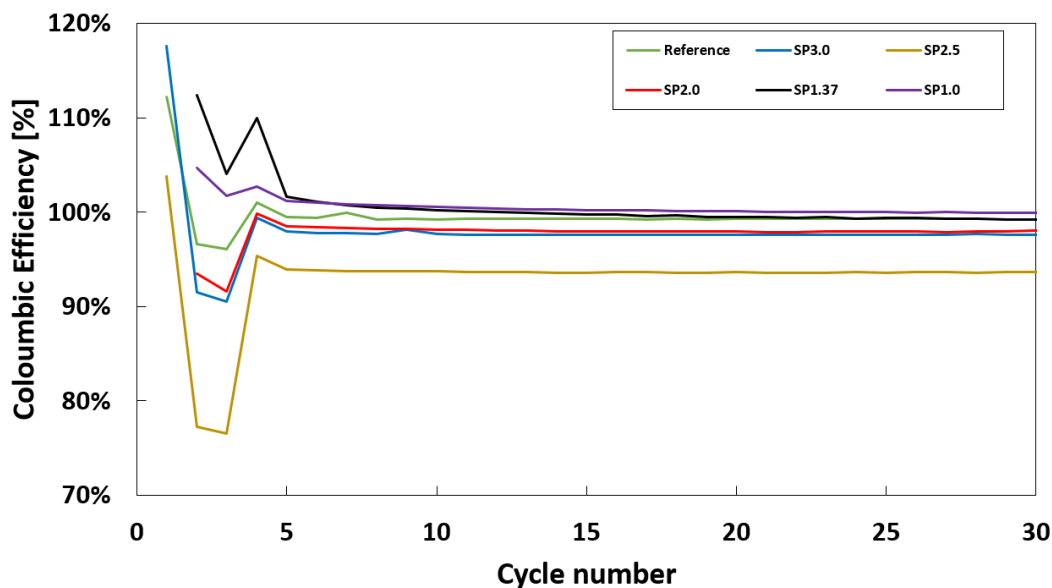
Figure 30: The coulombic efficiency of each sample during cycling.

Figure 31 shows how the internal resistance of each battery varies as the batteries are cycled up to 30 cycles. All samples, with the exception of SP1.0, show a similar initial internal resistance of approximately $40\,\Omega$. However, the samples display two distinct trends. The reference sample, SP3.0, and SP2.5 all display an increasing resistance from the 3rd cycle coinciding with a higher C-rate, from $\frac{C}{20}$ to $\frac{C}{5}$. After the initial jump the internal resistance for these samples slowly increase. The remaining samples, SP2.0 and SP1.37, both display a slowly decreasing internal resistance, with no apparent response to the change in C-rate.
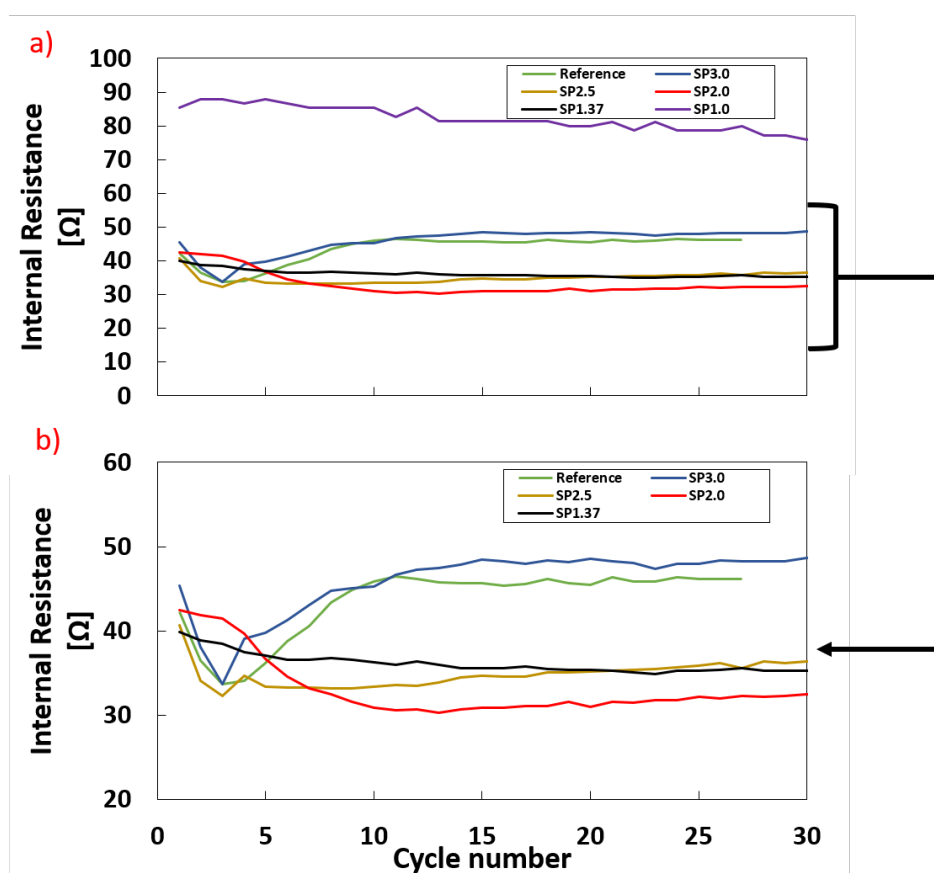
Figure 31: a) Shows the internal resistance for all samples during galvanostatic cycling. b) Shows the range from 20-60 Ω to clearly display the shape of the internal resistance curves. This excludes Sample 3.

Figure 32 shows $\frac{dQ}{dV}$ for the 20th cycle for each tested sample. Figure 33 shows a zoomed in version of Figure 32 where some of samples have been removed for clarity.
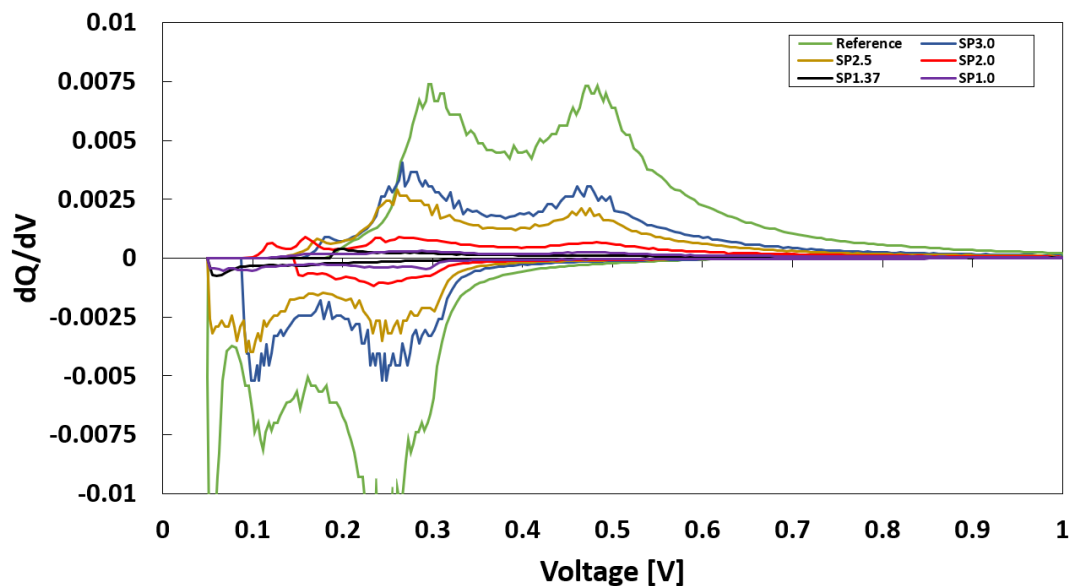
Figure 32: The figure shows $\frac{dQ}{dV}$ plots for cycle 20 for the galvanostatic cycling of samples.
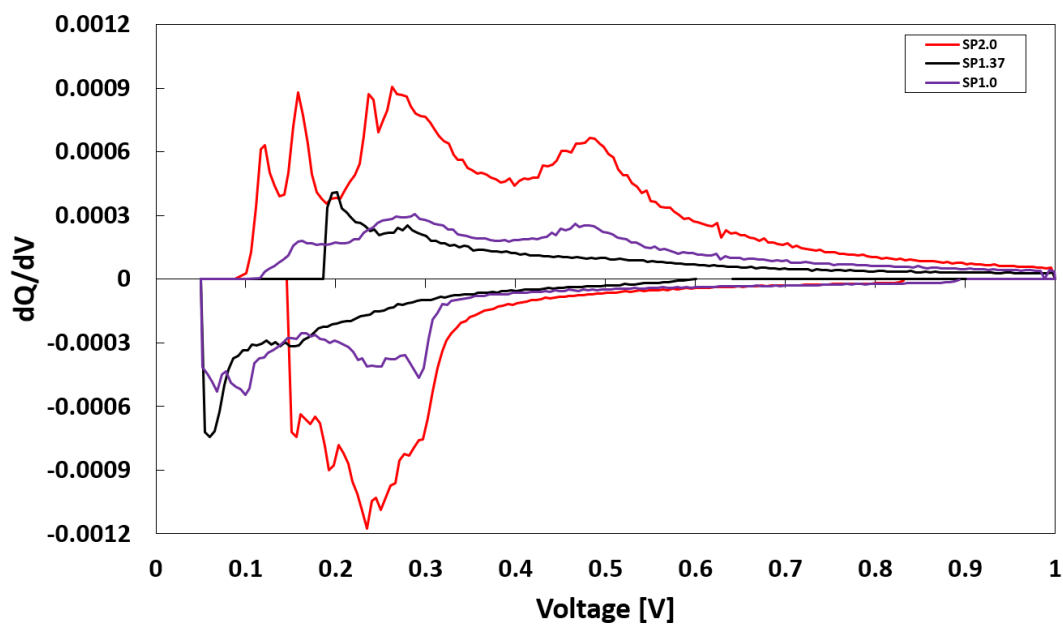
Figure 33: The figure shows $\frac{dQ}{dV}$ for cycle 20 plots for the galvanostatic cycling of samples. The Reference sample, Sample 8 and Sample 7 are excluded to show the shape of the $\frac{dQ}{dV}$ plots for the remaining three samples which display significantly lower magnitude $\frac{dQ}{dV}$ values.

4.2.3 Rate Testing

Rate testing was conducted as described in section 3.8 for each sample. The lines cut at the point where data had yet not been gathered at the time of writing.
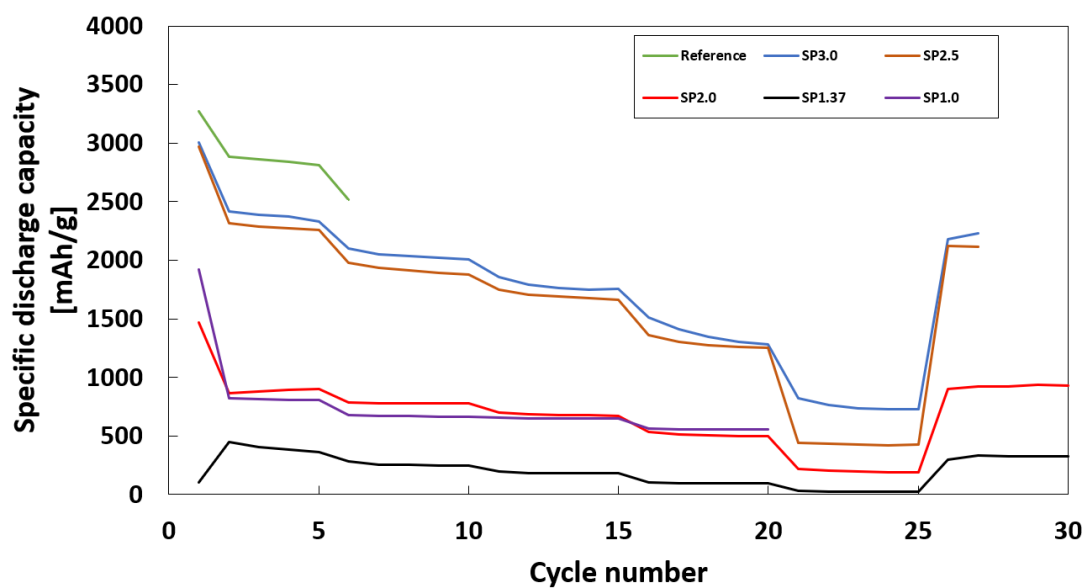
Figure 34: A plot of rate testing of the samples. The rate testing was performed as described in Section 3.8. Testing was done at c-rates of $\frac{C}{20}$, $\frac{C}{10}$, $\frac{C}{5}$, $\frac{C}{2}$, $1C$, and $\frac{C}{20}$ again.

5 Discussion

5.1 Discussing the Results from the Ball Milling Investigation

The specific discharge capacities displayed in Figure 19 show that the ball milling procedure reduces the initial specific discharge capacity for the tested Si types, with the exception of Nano-Si, which displays a modest increase (+8.8%). The initial capacity drops are most severe for a-Si (80.51%), but still significant in the cases of both Micro-Si (−39.51%) and Comm-Si (14.68%). The change in capacity retention after ball milling for the samples also differs between silicon types. Capacity retention after 150 cycles is improved for Micro-Si (+5.15%) and Comm-Si (+1.83%), but is reduced for a-Si (−41.33%) and Nano-Si (−21.86%) after ball milling. These results indicate that the specific properties of the powder in question affects how ball milling changes the anode performance of silicon, but does not allow for a simple conclusion regarding this relationship.

The CE of the initial cycling step provides insight into the surface of the active anode material as it largely depends on the extent of SEI formation which depends the surface area of the particles. In all cases the first cycle CE is reduced after ball milling, but a-Si displays a much larger decrease than the other silicon types.

The BET analysis indicates that the change in surface area is also not a simple relationship. Micro-Si (+24.27%) and Nano-Si (+16.68%) both display an modest growth in surface area after ball milling. Comm-Si shows a modest decrease (−26.14%) in surface area. However, a-Si shows a distinctly different behavior as the surface area increases manyfold after ball milling (+540.29%). The pore size increases for the silicon types which display an increased surface area and is reduced for Comm-Si, which also has a reduction in surface area. The exception is again a-Si which halves its pore size while the surface area increases significantly. This data indicates that the amorphous a-Si changes morphology through a different mechanism than its crystalline counterparts as its behavior is dissimilar to the other particles.

Combining the CE data with the surface area analysis a clear tendency that increased surface area causes reduced first cycle CE is seen in Figure 20, with the exception of Comm-Si where the surface area is reduced along with the CE. However, neither change is large in this case.

A possible explanation for the a-Si related observations is the oxidation of amorphous silicon during ball milling in an ambient atmosphere. During the ball milling procedure highly activated amorphous silicon surfaces are continuously created and oxidized. This gives a resulting sample of highly oxidized silicon which behaves differently from the crystalline silicon in the other samples. The silicon oxide has a low specific energy capacity which is seen in the galvanostatic cycling data from Figure 19. The oxidation of particles would expand their size and increase their surface area and may reduce the effect of cold welding of particles during ball milling.

5.2 Discussing the Results from the Carbon Coating Investigation

5.2.1 Identifying Polymer and Carbon Coating through SEM Images

The SEM is not an ideal tool to investigate the formation of a polymer coating or carbon coating to improve the performance of silicon as an anode. The target layer thickness is too low to be identified by the SEM, therefore some samples were coated with a large polymer fraction to test if the polymer was created and attached to the particles in a coating-like manner. This is the case specifically for SP1.0 and SP1.37. To look for signs of coating on the low polymer samples the main indication would be flimsy edges or a discernible change in the surface. The purpose of these images is to find an indication whether the silicon particles likely are coated, not to present certain proof that they are. This would require a TEM analysis.

The initial particles created had a low Si:polymer ratio and were not ball-milled. This was the case for the particles in the SEM and STEM images shown in Figure 23. The surface patterns observed are distinctly different from the pristine particles in Figure 21 indicating that polymer has attached to the surface. This theory is further reinforced by the STEM image which shows a porous layer that is partly penetrated by the electron beam. However, when inspecting the part of the particle towards the bottom edge of the image it appears as if the polymer coating is thicker and loses its characteristic pattern. This makes it problematic to determine if the particle is unique due to its low amount of polymer attached to its surface or if it is the only coated particle observed.

After seeing these results, it was proposed that some of the issue may be related to the sharp particle edges and large flat surfaces. It was suggested that ball milling the particles prior to coating may result in a particle morphology more suitable for polymer coating.

SEM images of Polymer Coated Silicon

Figure 24 shows the particles from Sample 2 and Sample 4 with a Si:polymer ratio of 0.5 and 1.37, respectively. Image a) shows Sample 2 and indicate that the particles have agglomerated into larger structure. However, whether this is a large polymer agglomerate with little silicon inside or an agglomerate with particles is difficult to determine. However, post carbonization, this polymer ratio proved difficult to work with as large, solid clumps of carbon and silicon were formed, and the samples' particles no longer had the required size to create a homogeneous anode slurry. Image b) shows Sample 4, where agglomerates have not formed in the same manner. However, many spherical structures are observed, which are likely silicon particles covered in polymer. This degree of spherical shape is not observed in any silicon particles in this size range, and the lack of a significant amount of other visible structures indicate that some of the spheres likely contain silicon particles.

However, when the Si:polymer ratio is increased to 3.00 as in Figure 25 a) or 2.50 as in the case of b), no visible change has occurred to the particles. The only arguments which suggest that these particles may have been coated in polymer is that the procedure is similar to that which coated the particles when a higher Si:polymer ratio, and the same reaction mechanisms should still apply.

SEM images of Carbon-Coated Silicon

Figure 27 a) shows a structure from Sample 4 post carbonization. At this stage, it seems apparent that the spherical structures have lost their smoothness and merged together with what appears to be a different material acting as a binding between particles. The surface of the particles now display distinct features. Note what appears like a flimsy layer at the edges of the structure. While not conclusive proof for the presence of carbon-coated silicon particles, this sample appears to be promising. Image b) is taken from the same sample. Here it is more difficult to recognize shapes which may be silicon particles and this may be a carbon piece with little or no silicon present. This image indicates that too much polymer has likely been added to this sample. Images c) and d) are both taken from Sample 3. The surface in c) displays features dissimilar from the pristine reference

post carbonization, but whether this is due to pieces of carbon attached to the surface or a layering is difficult to determine.

Figure 28 shows Sample 5 a) and Sample 7 b). Sample 7 has a lower polymer content and shows little deviation from the Reference sample. However, at a slightly higher polymer content in Sample 5 agglomerates form in with many small distinguishable particles in a manner not observed in the reference sample.

The conducted SEM analysis does not prove the existence of a carbon layer on the silicon particles. However, the samples with a low Si:polymer ratio display clear signs of the presence of carbon on the particles. The images do not provide sufficient information to conclude regarding the nature of this carbon or whether it forms a continuous layer. A more likely description based on this evidence is that the carbon gathers between silicon particles and interconnects them into large agglomerates.

5.2.2 Analyzing Galvanostatic Cycling of Samples with Varying Carbon Content

A Concern Regarding Capacity and C-rate

The main problem when investigating the galvanostatic cycling of these samples is related to the slurry composition and the determination of the capacity of the anode which is used for setting the C-rate. The reason this is an issue is that the silicon content present in each anode is uncertain. When making the slurry mixtures, the silicon added was assumed to be pure silicon. However, due to the addition of a significant mass of phenol some carbon will remain in the sample. This effect reduces the actual charge capacity of the sample, which in turn increases the experienced charge rate from the set value by an undetermined amount. This effect largely impacts samples with a low Si:polymer ratio as they have a larger carbon content. A higher C-rate reduces both the specific energy capacity and cycling stability of the sample. If it is assumed that a proportionate amount of silicon and carbon is lost throughout the process it is possible to calculate the actual silicon fraction and thus the amount of silicon in the sample. However, the carbon also has a specific storage capacity and its contribution to the overall capacity is difficult to determine.

Comments on the Results from Galvanostatic Cycling

From investigating the specific discharge capacity displayed in Figure 29, the initial observation is that with the exception of Sample 3 the first cycle discharge capacity decreases with added carbon content. This is expected as the carbon has a much lower specific capacity than the silicon and the charge rate at this stage is slow ($\frac{C}{20}$). However, the capacity retention after the 25th cycle is better than the Reference (62.48%) for Sample 8 (62.54%) and Sample 7 (67.39%). This demonstrates the expected trade-off for carbon coating of silicon, but a similar tendency might have been observed as a result of increased carbon content. Sample 6 displays a similar capacity retention (60.42%) while Sample 3 (33.63%) and 4 (21.14%) display low capacity retention. While the capacity retention judging from the initial cycle is only better than the reference for a selection of samples it is worth noting that the ICL from the fourth cycle and onward is reduced with lower Si:polymer ratio.

From the CE in Figure 30 no clear tendency is observed. SP2.5 exhibits a low CE while the remaining samples stabilize at a CE close to 100 %. All samples display an expected reduction in CE during the formation cycles. This is due to the consumption of charge for the formation of SEI.

The differences in resistances observed in Figure 31 may be partially explained by the increased carbon content. However, the abrupt change in behavior observed from SP3.0 to SP2.5 may be an indication that the carbon here contributes to lower the resistance so that it does not suddenly climb as the C-rate is increased. The high resistance observed for SP1.0 is likely due to an error introduced during cell fabrication. Similar outliers in terms of internal resistance are observed for some of the other tested samples as seen in Figure 38.

Interpreting Data from dQ/dV of the 20th Cycle

After 20 cycles the Reference samples clearly displays the four characteristic peaks for lithiation and delithiation of silicon. These peaks are visible for all tested samples with the exception of SP1.37. This indicates that these samples generate their specific capacity from the lithiation and delithiation of silicon, triggering the phase transformations in the material. For SP1.37 this plot along with the very low specific discharge capacity suggests that the silicon in the sample is not lithiated or delithiated to a significant extent. A small peak is observed corresponding to the formation of $Li_{15}Si_4$, but there is no indication of a transition to the fully lithiated state.

Comments on Rate Testing

The rate testing has been conducted for samples as described in Section 3.8 and the results are given in Figure 34. The results show the expected development as there are six plateaus corresponding to the varying C-rate used. The samples that have cycled to the end display a capacity regain, indicating that they have not lost their structure from the high rate cycling. As the C-rate increases the discharge capacity is reduced for all samples. Examining the transition from $\frac{C}{5}$ to $\frac{C}{2}$ SP3.0 loses 13.90% specific capacity, SP2.5 loses 18.37%, SP2.0 loses 24.55%, SP1.37 loses 40.60% and SP1.0 loses 12.79%. The expected result would be that the capacity loss is large for the samples with low carbon content and decreases for the samples with more carbon content. However, the results do not suggest that this is the case as no such trend is observed.

6 Conclusion

The main purpose of this work was to examine two techniques for mitigating the low cycling stability of silicon.

The first method that was examined was ball milling of silicon in air. Four different types of silicon were examined and the response to ball milling was discovered to be complex and highly dependent on the type of silicon. In most cases the initial specific discharge capacity was reduced with the increase in surface area due to the formation of additional SEI and in all cases the CE was reduced upon ball milling. However, the capacity retention was improved for all samples. The only amorphous sample tested, a-Si, displayed an enormous reduction in discharge capacity post ball milling and a large increase surface area. This was likely due to the severe oxidation of the amorphous surfaces during ball milling. The highest specific discharge capacity post ball milling was observed Comm-Si. Micro-Si displayed the highest capacity retention post ball milling, but the Comm-Si displays almost the same stability.

The second method that was examined was carbon coating of silicon with a phenol resin and carbonization at 820 °C. For low polymer content limited evidence was seen of polymer or carbon coating. However, the high polymer content samples show indications of coating or silicon particles agglomerated together by carbon. A range of Si:polymer ratios from 1 to 3 were tested. Lower Si:polymer ratio reduced the specific discharge capacity in all cases. However, gains were observed relative to the reference sample in terms of capacity retention for small amounts of added polymer. Lower Si:polymer ratios reduced the internal resistance. The $\frac{dQ}{dV}$ plots show that most samples are delithiated and lithiated with the expected phase transitions after 20 cycles. In the case of some of the samples peaks for lithiation of carbon are also evident.

To summarize, the ball milling behavior of different types of silicon were investigated. The research indicates that many factor affect the ball milling parameters and that amorphous silicon is poorly suited for ball milling in air. Carbon coating of silicon was attempted, but the result are not clear. Polymer was attached to the surface of silicon, but whether or not a continuous layer was established is unclear. Most of the evidence indicate that the added polymer acts as a binder material between silicon particles, forming agglomerates.

7 Further Work

Several ball milling experiments could be suggested to further this work. Investigating the ball milling of amorphous silicon in inert atmosphere would be an interesting experiment to evaluate what would happen in absence of oxygen. Optimizing ball milling procedures in terms of rpm, time, milling volume and ball-to-powder ratio is also necessary.

For the carbon coating investigation the most urgent further work is to assess the extent of carbon coating using a TEM. The high resolution images would allow for identification of carbon layers if they are present at the particle surfaces. After determining the success of the coating procedure further experiments may be conducted to determine the ideal Si:polymer ratio. In order to get an accurate C-rate the carbon fraction of carbonized samples may be identified by analyzing part of the sample in using TGA and flushing with air. The carbon would disappear, and the mass percent of silicon could be determined. Using these data the slurry composition could be adjusted accordingly to achieve the desired 60 wt% silicon. The results presented in this paper suggests that investigating the Si:polymer ratio larger than 2 would likely yield the best results.

After finding the ideal ratio experiments could be conducted with a different monomer, for example resorcinol. It would also be interesting to investigate the coating behaviour of the different silicon types considering the large differences in ball milling behaviour.

There is also a lot of room for optimizing the experimental procedure in terms of mixing times and temperatures. The amount of added formaldehyde and sodium hydroxide added to the solution would also be an interesting variable to investigate.

References

[1] Y. Meng, D. Gu, F. Zhang, Y. Shi, H. Yang, Z. Li, C. Y. B. Tu, and D. Zhao, "Ordered mesoporous polymers and homologous carbon framewors: Amphiphilic surfactant templating and direct transformation", *Angewandte Chemie - International Edition*, pp. 7215–7221, 2005.

[2] Z. Lu, B. Li, D. Yang, H. Lv, M. Xue, and C. Zhang, "A self-assembled silicon/phenolic resin-based carbon core-shell nanocomposie as an anode material for lithium ion batteries", *RSC Advances*, pp. 3477–3482, 2018.

[3] "The batteries report 2018", RECHARGE - The Advanced Rechargeable & Lithium Batteries Association, 2018. [Online]. Available: `https://www.rechargebatteries.org/`.

[4] R. V. and D. P. F., "Standards for the performance and durability assessment of electric vehicle batteries - possible performance criteria for an ecodesign regulation", European Union - JRC Technical Reports, 2018. [Online]. Available: `https://ec.europa.eu/jrc/en`.

[5] B. produced by the Eurpean Commission, "Towards the battery of the future", European Commission, 2018. [Online]. Available: `http://ec.europa.eu/environment/integration/research/newsalert/index_en.htm`.

[6] R. S. Treptow, "The lead-acid battery: Its voltage in theory and in practice", *Journal of Chemical Education*, vol. 79, no. 3, pp. 334–338, 2002.

[7] J. Pan, X. Zhang, Y. Sun, S. Song, W. Li, and P. Wan, "Preparation of high purity lead oxide from spent lead acid batteries via desulfurization and recrystallization in sodium hydroxide", *Industrial & Engineering Chemistry Research*, vol. 55, pp. 2059–2068, 2016.

[8] C. Liu, Y. Deng, J. Chen, D. Zou, and W. Su, "Integrated process to recover nimh battery anode alloy with selective leaching and multistage extraction", *Industrial & Engineering Chemistry Research*, vol. 56, pp. 7551–7558, 2017.

[9] G. Majeau-Bettez, T. R. Hawkins, and A. H. Strømman, "Life cycle environmental assessment of lithium-ion and nickel metal hydride batteries for plug-in hybrid and battery electric vehicles", *Applied Materials & Interfaces*, vol. 6, pp. 19 026–19 034, 2014.

[10] G. Kucinskis, G. Bajars, and J. Kleperis, "Graphene in lithium ion battery cathode materials: A review", *Journal of Power Sources*, vol. 240, pp. 66–79, 2013.

[11] N. Nitta, F. Wu, J. T. Lee, and G. Yushin, "Li-ion battery materials: Present and future", *Materials Today*, vol. 18, no. 5, pp. 252–264, 2015.

[12] M. Hannan, M. Lipu, A. Hussain, and A. Mohamed, "A review of lithium-ion battery state of charge estimation and management system in electric vehicle applications: Challenges and recommendations", *Renewable and Sustainable Energy Reviews*, vol. 78, pp. 834–854, 2017.

[13] D. Linden and T. B. Reddy, *Handbook of Batteries*, 3rd ed. McGraw-Hill, 2002.

[14] S. B. Chikkannanavar, D. M. Bernardi, and L. Liu, "A review of blended cathode materials for use in li-ion batteries", *Journal of Power Sources*, pp. 91–100, 2013.

[15] G. Patry, S. Martinet, and D. Froelich, "Cost modeling of lithium ion battery cells for automotive applications", *Energy Science and Engineering*, pp. 71–82, 2014.

[16] M. Létiche, M. Hallot, M. Huvé, T. Brousse, P. Roussel, and C. Lethien, "Tuning the cation ordering with the deposition pressure in sputtered $LiMn_1 \cdot 5 Ni_0 \cdot 5 O_4$ thin film deposited on functional current collectors for li-ion microbattery applications", *Journal of Chemical Education*, vol. 79, no. 3, pp. 334–338, 2002.

[17] J. R. Szczech and S. Jin, "Nanostructured silicon for high capacity lithium anodes", *Energy & Environmental Science*, vol. 56, no. 4, pp. 56–72, 2010.

[18] X. Zuoa, J. Zhua, P. Müller-Buschbaumb, and Y.-J. Chenga, "Silicon based lithium-ion battery anodes: A chronicle perspective review", *Nano Energy*, vol. 31, pp. 113–143, 2017.

[19] J. Kim, W. Choi, D. Byun, and J. K. Lee, "Electrochemical characteristics of phosphorus doped silicon for the anode material of lithium secondary batteries", *Solid State Ionics*, vol. 212, pp. 43–46, 2012.

[20] N. Takami, H. Inagaki, Y. Tatebayashi, H. Saruwatari, K. Honda, and S. Egusa, "High-power and long-life lithium-ion batteries using lithium titanium oxide anode for automotive and stationary power applications.", *Journal of Power Sources*, pp. 469–475, 2012.

[21] J.-T. Han and J. B. Goodenough, "3-v full cell performance of anod framework $TiNb_2O_7$/spinel$LiNi_0 \cdot 5\,Mn_1 \cdot 5\,O_4$", *Chemistry of Materials*, vol. 23, pp. 3404–3407, 2011.

[22] K. Xu, "Nonaqueous liquid electrolytes for lithium-based rechargeable batteries", *Chemistry Review*, vol. 104, pp. 4303–4417, 2004.

[23] X.-Q. Zhang, X. Chen, L.-P. Hou, B.-Q. Li, X.-B. Cheng, J.-Q. Huang, and Q. Zhang, "Regulating anions in the solvation sheath of lithium ions for stable lithium metal batteries", *ACS Energy Letters*, vol. 4, pp. 411–416, 2019.

[24] D. Aurbach, Y. Talyosef, B. Markovsky, E. Markevich, E. Zinigrad, L. Asraf, J. S. Gnanaraj, and H.-J. Kim, "Design of electrolyte solutions for li and li-ion batteries: A review", *Electrochimica Acta*, vol. 50, pp. 247–254, 2004.

[25] S. S. Zhang, "A review on electrolyte additives for lithium-ion batteries", *Journal of Power Sources*, vol. 162, pp. 1379–1394, 2006.

[26] J. Mindemark, L. Imholt, J. Montero, and D. Brandell, "Allyl ethers as combined plasticizing and crosslinkable side groups in polycarbonate-based polymer electrolytes for solid-state li batteries", *Journal of Polymer Science, Part A: Polymer Chemistry*, vol. 54, pp. 2128–2135, 2016.

[27] F. Zheng, M. Kotobuki, S. Song, M. O. Lai, and L. Lu, "A review on solid elecrolytes for all-solid-state lithium-ion batteries", *Journal of Power Sources*, vol. 389, pp. 198–213, 2018.

[28] N. Alias and A. A. Mohamad, "Advances of aqueous rechargeable lithium ion battery: A review", *Journal of Power Sources*, vol. 274, pp. 237–251, 2014.

[29] G. Zubi, R. Dufo-López, M. Carvalho, and G. Pasaoglu, "The lithium-ion battery: State of the art and future perspectives", *Renewable and Sustainable Energy Reviews*, vol. 89, pp. 292–308, 2018.

[30] A. Wang, S. Kadam, H. Li, S. Shi, and Y. Qi, "Review on modeling of the anode solid electrolyte interphase (sei) for lithium-ion batteries", *Nature: Computational Materials*, vol. 15, pp. 1–26, 2018.

[31] C. Chan, H. Peng, G. Liu, K. McIlwrath, Z. F. Zhang, R. A. Huggins, and Y. Cui, "High-performance lithium battery anodes using silicon nanowires", *Nature Nanotechnology*, pp. 31–35, 2008.

[32] F. Maroni, R. Raccichini, A. Birrozzi, G.Carbonari, R.Tossici, F.Croce, R.Marassi, and F.Nobili, "Graphene/silicon nanocomposite anode with enhanced electrochemical stability for lithium-ion battery applications", *Journal of Power Sources*, vol. 269, pp. 873–882, 2014.

[33] M. Gauthier, D. Mazouzi, D. Reyter, B. Lestriez, P. Moreau, D. Guyomard, and L. Roué, "A low-cost and high performance ball-milled si-based negative electrode for high-energy li-ion batteries", *Energy & Environmental Science*, vol. 6, pp. 2145–2155, 2013.

[34] D. Cui, F. Gao, and J. Qu, "Two-phase versus two-stage versus multi-phase liitiation kinetics in silicon", *Applied Physics Letters*, vol. 103, pp. 143 901–143 904, 2013.

[35] S. Hansen, E. Quiroga-González, J. Carstensen, and H. Föll, "Size-dependent cyclic voltammetry study of silicon microwire anodes for lithium ion batteries", *Electrochimica Acta*, vol. 217, pp. 283–291, 2016.

[36] S. C. Jung and Y.-K. Han, "Ab initio molecular dynamics simulation of lithiation-induced phase-transition of crystalline silicon", *Electrochimica Acta*, vol. 62, pp. 73–36, 2012.

[37] K. Ogata, E. Salager, C. Kerr, A. Fraser, C. Ducati, A. Morris, S. Hofmann, and C. Grey, "Revealing lithium-silicide phase transformations in nano-structued silicon-based lithium ion batteries via in situ nmr spectroscopy", *Nature Communications*, vol. 248, pp. 91–100, 2014.

[38] S. H. Kim, Y. S. Kim, W. J. Baek, S. H. andDong-Jin Yun, S. Han, and H. Jung, "Nanoscale electrical degradation of silicon-carbon composite anode materials for lithium ion batteries", *Applied Materials & Interfaces*, vol. 10, pp. 24 549–24 553, 2018.

[39] Y. Bie, J. Yu, J. Yang, W. Lu, Y. Nuli, and J. Wang, "Porous microspherical silicon composite anode material for lithium ion battery", *Electrochimica Acta*, vol. 178, pp. 65–73, 2015.

[40] R. C. de Guzman, J. Yang, M. M. Cheng, S. O. Salley, and K. S. Ng, "Effects of graphene and carbon coating modifications on electrochemical performance of silicon nanoparticle/graphene composite anode", *Journal of Power Sources*, vol. 246, pp. 335–345, 2013.

[41] A. F. Gonzalez, N.-H. Yang, and R.-S. Liu, "Silicon anode design for lithium-ion batteries: Progress and perspectives", *The Journal of Physical Chemistry*, vol. 121, pp. 27 775–27 787, 2017.

[42] Murugesan, J. T. Harris, B. A. Korgel, and K. J. Stevenson, "Copper-coated amorphous silicon particles as an anode material for lithium-ion batteries", *Chemistry of Materials*, vol. 24, pp. 1306–1315, 2012.

[43] S. Rajeshkanna and O. Nirmalkumar, "Synthesis and characterization of cu nanoparticles using high energy ball milling route and compare with scherrer equation", *International Journal of Scientific Enfineering and Research*, vol. 2, pp. 30–35, 2014.

[44] J. Zhang, Z. Shi, and C. Wang, "Effect of pre-lithiation degrees of mesocarbon microbeads anode on the electrochemical performanc eof lithium-ion capacitors", *Electrochimica Acta*, vol. 125, pp. 22–28, 2014f.

[45] F. Holtstiege, P. Bärmann, R. Nölle, M. Winter, and T. Placke, "Pre-lithiation strategies for rechargeable energy storage technologies: Concepts, promises and challenges", *Batteries*, vol. 4, pp. 1–39, 2018.

[46] Y. Domi, H. Usui, M. Shimizu, Y. Kakimoto, and H. Sakaguchi, "Effect of phosphorus-doping on electrochemical performance of silicon negative electrodes in lithium-ion batteries", *Applied materials & Interfaces*, vol. 4, no. 8, pp. 7125–7132, 2016.

[47] T. Mongstad, H. Andersen, J. Mæhlen, W. Filtvedt, H. Klette, Ø. Nordseth, and M. Kirkengen, "No significant effect of phosphorus doping on the electrochemical performance of silicon-carbon composite anodes for li-ion batteries", in *ECS Transactions*, The Electrochemical Society, Kjeller, Norway: Institute for Energy Technology, 2016, pp. 275–280.

[48] M. ho Kong, J. hyun Noh, D. jin Byun, and J. kee Lee, "Electrochemical characteristics of phosphorus doped silicon and graphite for the anode materials of lithium secondary batteries", *Journal of Electroceramics*, vol. 23, pp. 376–381, 2008.

[49] S. Huang, L. zhi Cheong, D. Wang, and C. Shen, "Nanostructured phosphorus doped silicon/graphite composite as anode for high-performance lithium-ion batteries", *Applied materials & Interfaces*, vol. 9, pp. 23 672–23 678, 2017.

[50] Z. Jiao, Y. Gao, S. Liu, S. Huang, Y. Jiang, Z. Chen, and B. Zhao, "Controlled scalable synthesis of yolk-shell structured large-size industrial silicon with interconnected carbon network for lithium storage", *Electrochimica Acta*, vol. 283, pp. 1702–1711, 2018.

[51] A. Soam, P. Kavle, A. Kumbhar, and R. O. Dusane, "Performance enhancement of micro-supercapacitor by coating of graphene on silicon nanowires at room temperature", *Current Applied Physics*, vol. 17, pp. 314–320, 2016.

[52] T. Jaumann, M. Herklotz, M. Klose, K. Pinkert, S. Oswald, J. Eckert, and L. Giebler, "Tailoring hollow silicon-carbon nanocomposite as high-performance anodes in secondary lithium-based batteries through economical chemistry", *Chemistry and Materials*, vol. 27, pp. 37–43, 2015.

[53] Y. Chen, Y. Hu, J. Shao, Z. Shen, R. Chen, X. Zhang, X. He, Y. Song, and X. Xing, "Pyrolytic carbon-coated silicon/carbon nanofiber composite anodes for high-performance lithium-ion batteries", *Journal of Power Sources*, vol. 298, pp. 130–137, 2015.

[54] M.-F. Grenier-Loustalot, S. Larroque, P. Grenier, J.-P. Leca, and D. Bedel, "Phenolic resins: 1. mechanisms and kinetics f phenol and of the first polycondensates towards formaldehyde in solution", *POLYMER*, vol. 35, no. 14, pp. 324–338, 1994.

[55] X. Zhao, S. Niketic, C.-H. Yim, J. Zhou, J. Wang, and Y. Abu-Lebdeh, "Revealing the role of poly(vinylidene fluoride) binder in si/graphite composite anode for li-ion batteries", *ACS Omega*, vol. 3, pp. 11 684–11 690, 2018.

[56] P. Parikh, M. Sina, A. Banerjee, X. Wang, M. S. D'Souza, J.-M. Doux, E. A. Wu, O. Y. Trieu, Y. Gong, Q. Zhou, K. Snyder, and Y. S. Meng, "Role of polyacrylic acid (paa) binder on the solid electrolyte interphase in silicon anodes", *Chemistry of Materials*, vol. 31, pp. 2535–2544, 2019.

[57] S. Y. Lai, K. D. Knudsen, B. T. Sejersted, A. Ulvestad, J. P. Mæhlen, and A. Y. Koposov, "Silicon nanoparticle ensembles for lithium-ion batteries elucidated by small angle neutron scattering", *Applied Energy Materials*, pp. 3220–3227, 2019.

[58] J. M. Zielinski and L. Kettle, *Physical characterization: Surface area and porosity*, Whitepaper, Intertek, 2013.

8   Appendices

1. **Brunauer-Emmett-Teller Analysis (BET)**
2. **Derivation of the BET-isotherm**
3. **Flow Chart of the Experimental Procedure for Carbon Coating**
4. **Galvanostatic Cycling Data for All Samples**
5. **Supplementary SEM images**

8.1 Brunauer-Emmett-Teller Analysis (BET)

BET analysis is the standard method for determining the surface area of powders. By exposing the powder to an inert gas which adsorbs to the powders surface and knowing the saturation pressure of the gas, the volume of gas inserted and measuring the pressure it is possible to determine the surface area of the powder through the BET-isotherm relation as expressed in Equation 5 and derived in Appendix section 8.2.

$$\frac{1}{v(\frac{p_0}{p} - 1)} = \frac{c-1}{v_m c}(\frac{p}{p_0}) + \frac{1}{v_m c} \tag{5}$$

Here c is a constant dependent on the gas properties given by $c = exp(\frac{E_1 - E_L}{RT})$. By plotting $\frac{1}{v(\frac{p_0}{p} - 1)}$ against $\frac{p_0}{p}$ a straight line results for small $\frac{p_0}{p}$ values. If the slope of the line is A and $c = 1 + \frac{A}{I}$ then the total surface area is given by Equation 6.

$$S_{tot} = \frac{v_m N s}{V} \tag{6}$$

Typically, nitrogen is the gas of choice for BET-analysis. However, other gases that do not react with the sample may be used.

To evaluate the porosity of a sample the relative pressure $\frac{p_0}{p}$ is increased beyond the formation of a monolayer. Capillary forces trigger condensation of the inert gas as the small pores in the material is filled. As the relative pressure is further increased the larger pores in the material is also filled with the liquid condensed gas and as the relative pressure approaches 1 all pores are treated as filled. By knowing the density of the liquid gas the pore volume may then be calculated. Additional information regarding pore sizes and the pore network connectivity may be extracted by evaluating the slope and the hysteresis of the adsorption and desorption lines in a relative pressure versus gas loading [$cm^3\,g^{-1}$] plot[58].

The data from BET is limited due to the assumptions made in the derivation of the BET isotherm, these assumptions are listed in section 8.2.

8.2 Derivation of the BET isotherm

Deriving the Brunauer-Emmett-Teller equation may be done through the following steps:

1. Define the surface area covered by $0, 1, 2, 3, ..., n$ layers of adsorbed molecules as $\theta_0, \theta_1, \theta_2, \theta_3, ..., \theta_n$. In addition, the total surface area and the total volume of adsorbed particles is defined as given in Equation 7 and 8

$$A_{tot} = \sum_{i=0}^{\infty} \theta_i \tag{7}$$

$$V_{tot} = V_0 \sum_{i=0}^{\infty} i\theta_i \tag{8}$$

2. Assuming the system is in a state of equilibrium then the surface area covered by a single layer of adsorbed atoms must be a constant. Hence, θ_0 is a constant and the rate of evaporation from the first layer must be equal to the rate of condensation onto the bare surface such that Equation 9 is fulfilled.

$$k_{-1}\theta_1 = k_1 P \theta_0 \tag{9}$$

Where P is the pressure, and k_1 and k_{-1} are rate constants for evaporation and condensation.

3. Applying the same equilibrium conditions to further layers it is evident that for the first layer θ_1 must also be constant. Then the sum of condensation on the bare surface and the rate of evaporation from the second layer is equal to the sum of the rate of condensation onto the firs later and the rate of evaporation from the second layer. Hence, the relation given in Equation 10.

$$k_1 P\theta_0 + k_{-2}\theta_2 = k_2 P\theta_1 + k_{-1}\theta_1 \tag{10}$$

Combining with Equation 9 this is simplified to Equation 11.

$$k_{-2}\theta_2 = k_2 P\theta_1 \tag{11}$$

This leads to the general conclusion that every layer may be related to the preceding layer through Equation 12.

$$k_{-i}\theta_i = k_i P\theta_{i-1} \tag{12}$$

4. From combining Equation 7 and 8 the relationship between total area covered and the total volume of gas may be presented as in Equation 13.

$$\frac{v}{Av_0} = \frac{v}{v_m} = \frac{\sum\limits_{i=0}^{\infty} i\theta_i}{\sum\limits_{i=0}^{\infty} \theta_i} \tag{13}$$

Where v_m is the volume of gas corresponding to a monolayer covering the entire surface area and v_0 is the volume of gas corresponding to a monolayer on one cm^2.

5. By re-organizing and simplifying by introducing $y = \frac{k_1}{k_{-1}}P$ Equation 9 may be expressed as Equation 14.

$$\theta_1 = y\theta_0 \tag{14}$$

This conclusion may be generalized for each layer as in Equation 15.

$$\frac{k_{-2}}{k_2}...\frac{k_{-i}}{k_i} = g \tag{15}$$

6. By defining a new quantity $x = \frac{P}{g}$ we have $\theta_2 = x\theta_1$ and $\theta_3 = x\theta_2 = x^2\theta_1$ which may be generalized by introducing $c = \frac{x}{y}$ as in Equation 16.

$$\theta_i = x\theta_{i-1} = x^{i-1}\theta_1 = x^{i-1}y\theta_0 \tag{16}$$

Combining with Equation 13 we may expand the expression as shown in Equation 17

$$\frac{v}{v_m} = \frac{\sum\limits_{i=0}^{\infty} i\theta_i}{\sum\limits_{i=0}^{\infty} \theta_i} = \frac{c\theta_0 \sum\limits_{i=0}^{\infty} ix_i}{\theta_0 + \theta_1 + \theta2 + ...} = \frac{c\theta_0 \sum\limits_{i=1}^{\infty} ix_i}{\theta_0(1 + c\sum\limits_{i=1}^{\infty} x_i)} = \frac{c\sum\limits_{i=1}^{\infty} ix_i}{(1 + c\sum\limits_{i=1}^{\infty} x_i)} \tag{17}$$

7. In order to simplify the expression further take advantage of the properties of infinite geometric series. These are $\sum\limits_{i=1}^{\infty} x_i = \frac{x}{1-x}$ and $\sum\limits_{i=1}^{\infty} ix_i = x\frac{d}{dx}\left(\frac{x}{1-x}\right) = \frac{x}{(1-x)^2}$. Which allows the simplification of Equation 17 as shown in Equation 18.

$$\frac{v}{v_m} = \frac{cx}{(1-x)^2}\frac{1}{1+\frac{cx}{1-x}} = \frac{cx}{\frac{(1-x)^2(1-x+cx)}{1-x}} = \frac{cx}{(1-x)(1-x+cx)} \tag{18}$$

8. When the pressure is equal to the saturation pressure ($P = P_0$) an infinite number of adsorbate layers build up such that Equation 18 must approach infinite. This is achieved when $x = 1$ at P_0 then $g = P_0$ and $x = \frac{P}{P_0}$ such that v may be expressed as the BET isotherm in recognizable form as in Equation 19.

$$v = \frac{v_m c x}{(1-x)(1+(c-1)x)} \rightarrow \frac{x}{v(1-x)} = \frac{1}{v_m c} + \frac{x(c-1)}{v_m c} \tag{19}$$

8.3 Flow Chart of the Experimental Section for Carbon Coating
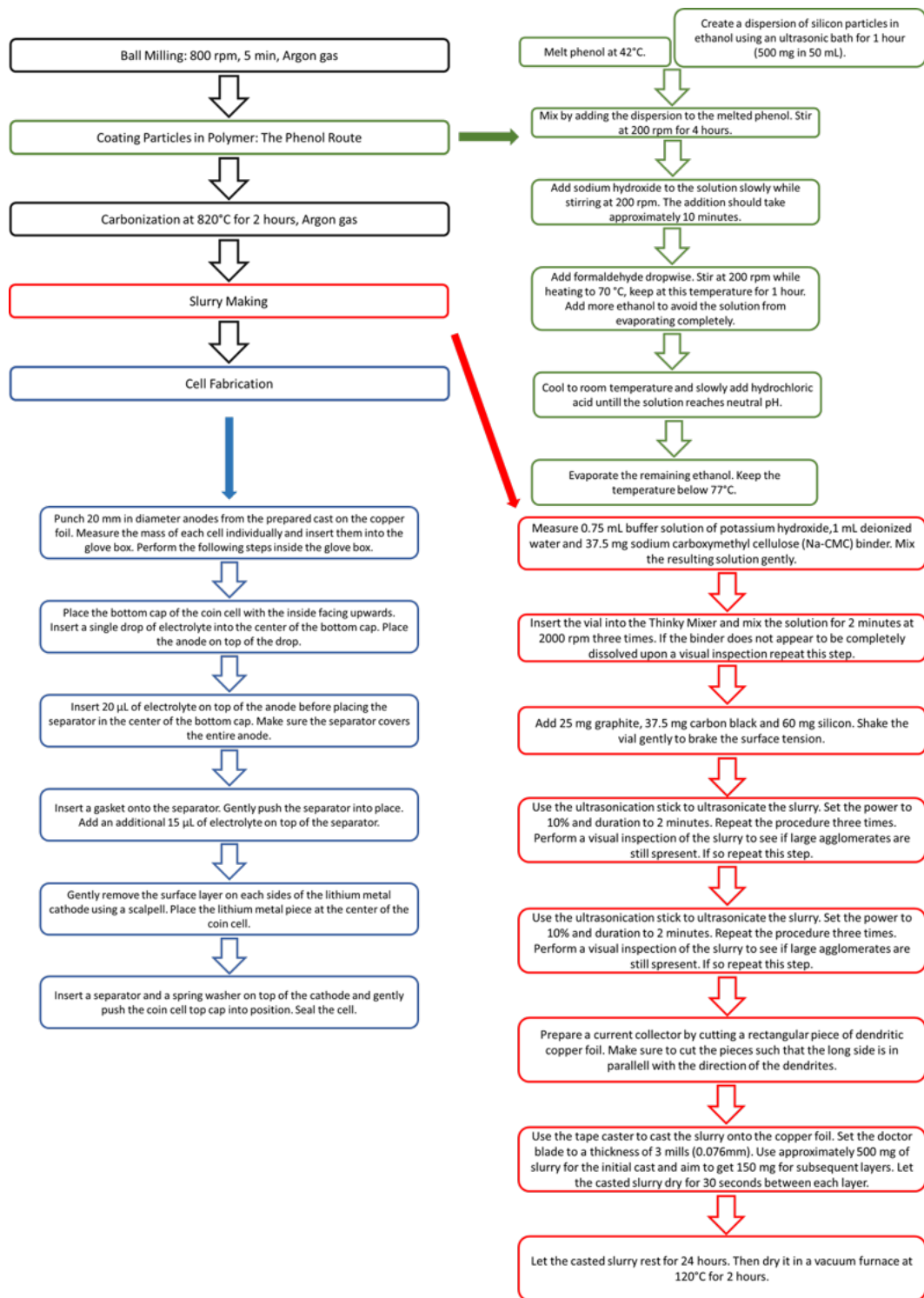
Figure 35: A flow chart illustrating the steps in the experimental procedure used for carbon coating.
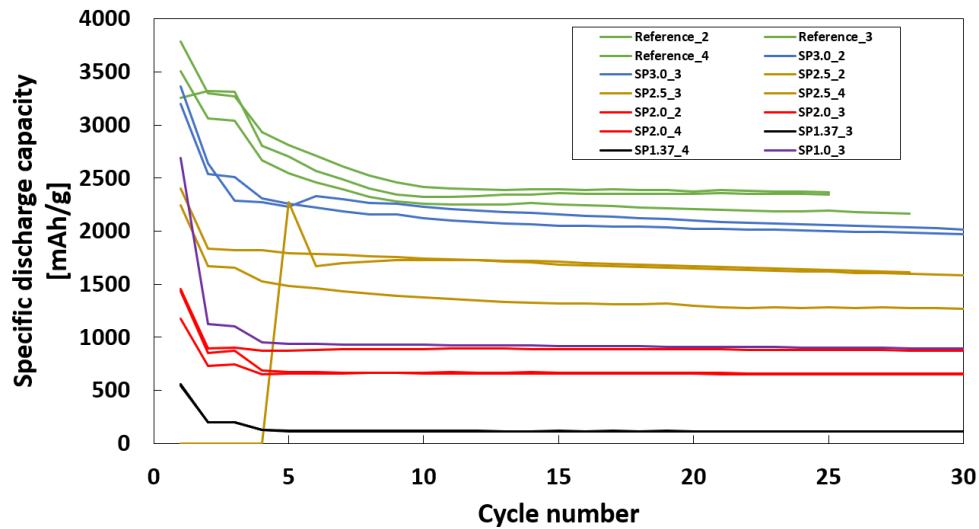
8.4 Galvanostatic Cycling Data for All Samples

Figure 36: The total cycling discharge data for all tested cells for the 30 first cycles. Samples were discharged to maximum capacity.
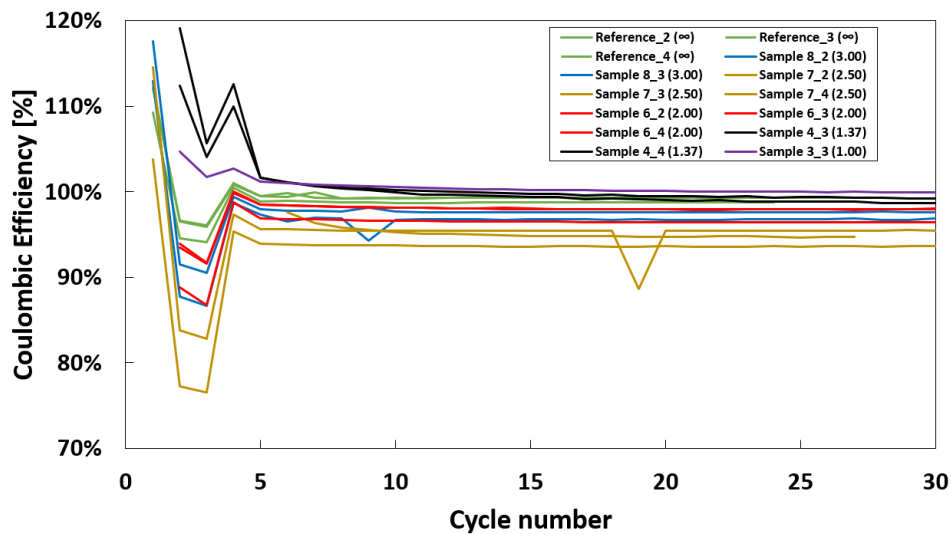

Figure 37: The total cycling coulombic efficiency data for all tested cells for the 30 first cycles. Samples were discharged to maximum capacity.
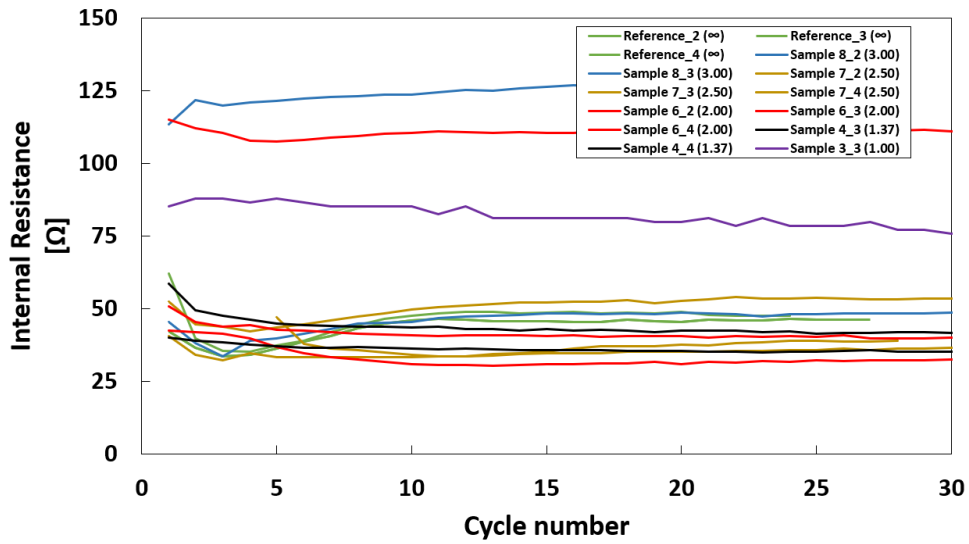
Figure 38: The total cycling internal resistance data for all tested cells for the 30 first cycles. Samples were discharged to maximum capacity.
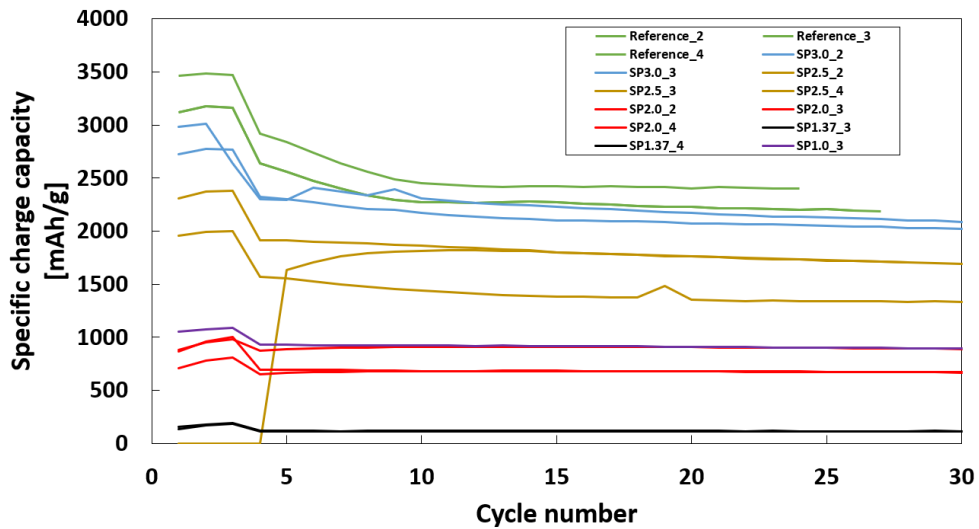

Figure 39: The total cycling charge data for all tested cells for the 30 first cycles. Samples were discharged to maximum capacity.